3-2021

Studying the Conditions for Magnetic Reconnection in Solar Flares with and without Precursor Flares

Seth H. Garland

Studying the Conditions for Magnetic Reconnection in Solar Flares with and without Precursor Flares

THESIS

Seth H. Garland, Capt, USAF

AFIT-ENP-MS-21-M-117

DEPARTMENT OF THE AIR FORCE
AIR UNIVERSITY

AIR FORCE INSTITUTE OF TECHNOLOGY

Wright-Patterson Air Force Base, Ohio

AFIT-ENP-MS-21-M-117

STUDYING THE CONDITIONS FOR MAGNETIC RECONNECTION IN SOLAR FLARES WITH AND WITHOUT PRECURSOR FLARES

THESIS

Presented to the Faculty

Department of Engineering Physics

Graduate School of Engineering and Management

Air Force Institute of Technology

Air University

Air Education and Training Command

in Partial Fulfillment of the Requirements for the

Degree of Master of Science in Applied Physics

Seth H. Garland, B.S.

Capt, USAF

March 2021

AFIT-ENP-MS-21-M-117

STUDYING THE CONDITIONS FOR MAGNETIC RECONNECTION IN SOLAR FLARES WITH AND WITHOUT PRECURSOR FLARES

THESIS

Seth H. Garland, B.S.
Capt, USAF

Committee Membership:

Robert D. Loper, Ph.D.
Chair

Maj Daniel J. Emmons, Ph.D.
Member

AFIT-ENP-MS-21-M-117

Abstract

Forecasting of solar flares remains a challenge due to the limited understanding of the triggering mechanisms associated with magnetic reconnection, the primary physical phenomenon connected to these events. Consequently, forecasting methods continue to rely on climatological patterns of solar flare events as opposed to the underlying physics principles. Models of magnetic reconnection in the solar atmosphere places the null point of the reconnection within the corona. Though it is difficult to directly measure the magnetic field parameters in the solar corona, the coronal magnetic fields are tied to the photospheric magnetic fields, which are much easier to measure directly. Studies have indicated that changes to the photospheric magnetic fields – particularly in relation to the field helicity – occur during solar flare events, associated with magnetic reconnection. This study utilized data from the Solar Dynamics Observatory (SDO) Helioseismic and Magnetic Imager (HMI) and SpaceWeather HMI Active Region Patches (SHARPs) to analyze full vector-field component data of the photospheric magnetic field during solar flare events within a near decade long HMI dataset. Analysis of the data was used to identify and compare the trends of differing flare classes for varying time intervals leading up to an event, as well as the trends of flares that occur with and without a precursor flare, in order to discern signatures of the physical mechanisms involved.

Acknowledgements

First, I would like to thank my family for supporting me throughout my study. Their constant words of encouragement kept my motivation high, helping me to get all my work done in a timely manner. I would especially like to thank my wife for always listening to my ramblings regarding the research, as well as keeping me on track if I ever started to veer.

I would also like to thank my classmates, in particular 1st Lt Brian Kay and 1st Lt Rodney Carmona, not only for their reviews of my work, but also the much needed comedic relief they provided to survive the more stressful moments. My time at AFIT would not have been the same without their friendship.

Lastly, I would like to thank my advisor for his mentoring and guidance during the last two years. Additionally, I'd like to thank my committee for their enthusiasm for my work and devotion to assisting me. Both Dr. Loper and Maj Emmons have taught me a great deal about space weather in general, as well as potential career paths in such a field.

Seth H. Garland

Table of Contents

List of Figures

List of Tables

List of Abbreviations

AR active region

CME coronal mass ejections

DoD Department of Defense

EM electromagnetic

GOES Geostationary Operational Environmental Satellite

GWILL gradient-weighted inversion-line length

HAO High Altitude Observatory

HARP HMI Active Region Patch

HF high frequency

HMI Helioseismic and Magnetic Imager

JSOC Joint Science Operations Center

LMSAL Lockheed Martin Solar and Astrophysics Laboratory

LoS line-of-sight

LWS Living With a Star

MDI Michelson Doppler Imager

MHD magnetohydrodynamic

NASA National Aeronautics and Space Administration

NOAA National Oceanic and Atmospheric Administration

NRT near-real time

PIL primary inversion line

RHESSI Reuven Ramaty High Energy Solar Spectroscopic Imager

SDO Solar Dynamics Observatory

SHARP Space Weather HMI Active Region Patch

SID Sudden Ionospheric Disturbance

SOHO Solar and Heliospheric Observatory

SWPC Space Weather Prediction Center

TAI International Atomic Time

UTC Coordinated Universal Time

I. Introduction

A solar flare is an intense burst of radiation, across the entire electromagnetic (EM) spectrum, that results from the release of magnetic energy from highly concentrated magnetic fields associated with active regions (ARs) on the Sun's surface. Solar flares are classified based on their peak flux in the soft x-ray wavelength range of 1 – 8 $\mathring{A}$ (see Table 1). A typical flare will release approximately 10^{22} joules of energy, while a strong flare will release approximately 10^{25} joules, equivalent to 2.4 x 10^{15} tons of TNT. The energy released by a solar flare can result in direct plasma heating, produce strong mass motions, accelerate particles, and produce magnetohydrodynamic (MHD) waves that are believed to heat the solar corona and accelerate the solar wind (Antiochos and DeVore, 2008).

Table 1. Solar Flare Classifications

Flare Class	Peak Flux in wavelengths 1 - 8 Å, *I* (W/m^2)
A	$10^{-8} \leq I < 10^{-7}$
B	$10^{-7} \leq I < 10^{-6}$
C	$10^{-6} \leq I < 10^{-5}$
M	$10^{-5} \leq I < 10^{-4}$
X	$10^{-4} \leq I$

Space weather – i.e., solar flares, coronal mass ejections (CMEs), geomagnetic storms, etc. – is of rising importance as a severe risk recognized by governmental agencies, including the Department of Defense (DoD) and corporations, as humankind's utilization of/dependence on technology continues to grow (Eastwood et al., 2017). The accelerated,

energetic particles and increased EM radiation from solar flares create disturbances in the Earth's magnetic and electric fields, as well as its atmosphere, which can result in degraded performance or damage of equipment, both on Earth and in the space environment. Specifically, induced currents associated with CMEs may damage physical infrastructure (particularly transformers); the heating and resulting expansion of the atmosphere by flares will increase drag on satellites, leading to greater expenditure of fuel to correct course; and surface or internal dielectric charging of satellites by energetic particles can cause intermittent anomalous behavior or complete satellite failure (Eastwood et al., 2017). Additionally, increases in the ionospheric ionization – called Sudden Ionospheric Disturbances (SIDs) – causes scintillation or complete absorption of high frequency (HF) radio waves that leads to degradation or loss of satellite communication. It is estimated that a solar flare and associated solar radiation storm of similar magnitude to the Carrington Event of 1859 would cause such catastrophic damage that it would take approximately 4 – 10 years to recover (Eastwood et al., 2017). A separate assessment of a Carrington level event estimated a total economic cost of $0.6 – 2.6 trillion in the United States alone, assuming power outages lasting one to two years (Eastwood et al., 2017). More important than the threat solar flares post to equipment is the threat to personnel in high altitude aircraft and spacecraft that would be exposed to the enhanced levels of radiation. Reduced flight times at high altitudes would be required in order to avoid reaching radiation dose limits, which would have a huge operational impact in the form of delays and increased fuel use from rerouting flights.

Given the potentially severe impacts to personnel and equipment from the effects of solar flares, and the fact that these effects only take eight minutes to reach the Earth

following a flare occurrence (i.e., there is no detection lead time), it is critical that solar flare events be forecasted. Due to the limited understanding of the underlying physical processes of these events, forecasting methods continue to rely on climatological patterns and rules of thumb, e.g., flare persistence which states that an AR that has flared recently is likely to flare again (Sawyer et al., 1986). McIntosh (1990) created probabilistic forecasts for flares by applying Poisson statistics to observations of flare production rates for different classes of active regions. Forecasts published today – including those from the Space Weather Prediction Center (SWPC) – use this approach as a basis (Leka et al., 2018). Several studies that have utilized various statistical methods and machine-learning/discriminant analysis algorithms for flare forecasting (Bobra and Couvidat, 2015; Leka et al., 2018; Mason and Hoeksema, 2010) found that such methods produced little to no improvement in forecasting ability over climatology. In fact, the results of a workshop held in Boulder, CO in 2009 – where the performance of 11 different statistical flare forecasting methods/algorithms was compared on a common dataset from the Solar and Heliospheric Observatory/Michelson Doppler Imager (SOHO/MDI) – showed that (1) no one method clearly outperformed all others, and (2) no method was substantially better than climatological forecasts (Barnes et al., 2016). Improvement of flare forecasting ability will only be achieved with a better understanding of the trigger mechanism associated with solar flare occurrence.

Magnetic reconnection – i.e., the joining of antiparallel magnetic field lines – is widely believed to be such a trigger mechanism, responsible for the eruptive release of energy involved with solar flares. The general two-dimensional setup for magnetic reconnection can be seen in Figure 1, where antiparallel magnetic fields that lie on either

side of a resistive current sheet diffuse into the sheet, cancelling each other out, and converting the magnetic energy into kinetic/thermal energy (Russell et al., 2016).

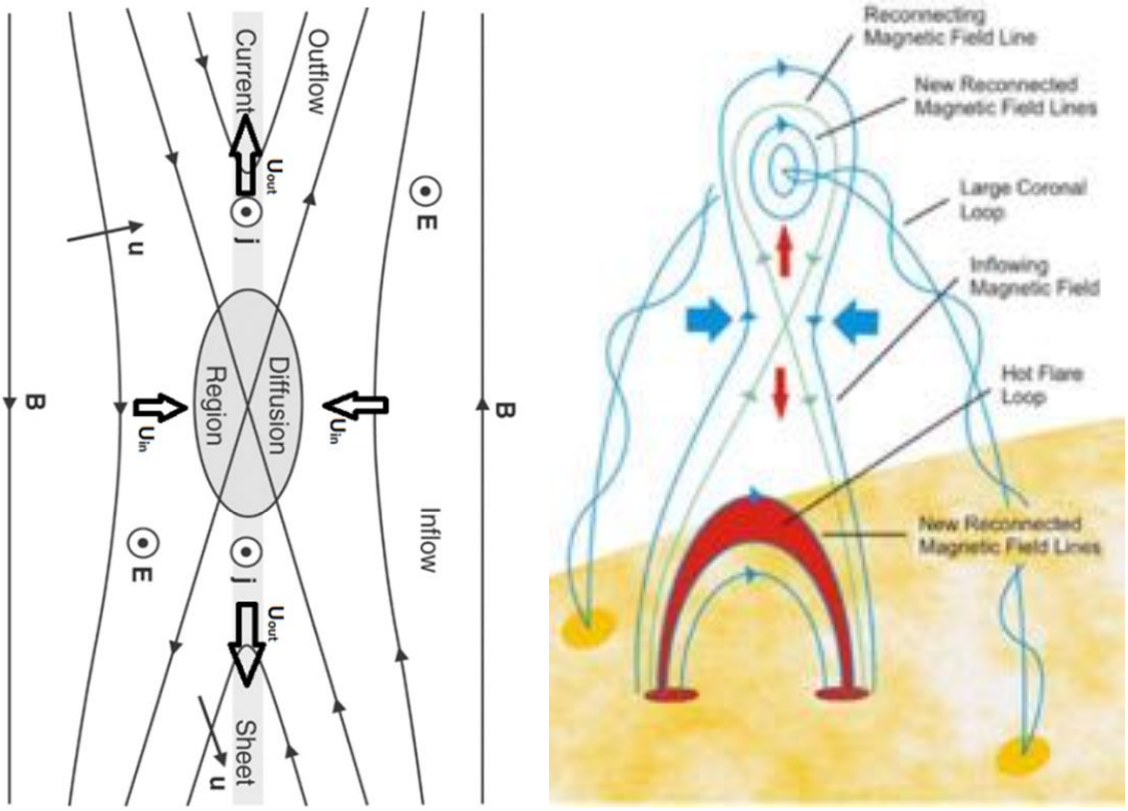

Figure 1. General setup for magnetic reconnection (Left image adapted from Russell et al., 2016; right image courtesy of NASA). Arrowed lines are the magnetic field (B) lines, E is the electric field, j is current density, and u is the plasma velocity.

The outline of the solar flare process involving reconnection is (Antiochos and DeVore, 2008; Priest and Forbes, 2002):

(1) A sheared and stressed magnetic field slowly emerges from below the photosphere and rises into a coronal arcade containing a prominence, building up free energy in the corona.

(2) Magnetic reconnection acts as a triggering mechanism that destroys the magnetic equilibrium of the corona, leading to an explosive instability.

(3) The magnetic field erupts outward, ejecting and accelerating the plasma.

(4) Further reconnection closes the field back down to a less stressed state, and magnetic energy is converted, resulting in the heating of the plasma and an intense x-ray burst.

Essentially, once the magnetic field over an AR becomes sheared and twisted to a certain point, magnetic reconnection "turns on" to alleviate the magnetic stress, causing the initial eruption and loss of equilibrium of the field; however, continued reconnection of the field lines rapidly restores equilibrium and brings the field into a less stressed configuration.

Models of magnetic reconnection still do not accurately predict the rate at which reconnection occurs during a solar flare event. One of the original models, the Sweet-Parker Model, employs a current sheet that stretches the entire length of the boundary between antiparallel magnetic fields, with field lines diffusing into the sheet at the same rate they diffuse out. However, the resulting rate of reconnection this model predicts is far too slow to represent a solar flare (Priest and Forbes, 2002). The Petschek model utilizes a smaller current sheet that divides into two pairs of slow-mode shocks, resulting in reconnection rates that accurately represent chromospheric reconnection (Chae et al., 2002; Priest and Forbes, 2002). Antiochos and DeVore (2008) describe the tether-cutting and breakout models which focus on redistributing the shear within a sheared region of the magnetic field so that it is concentrated on the outermost field lines at the edge of the sheared region. If the transfer of the shear is sufficiently rapid, then the eruptive behavior of a solar flare should occur.

To continue the improvement of magnetic reconnection models – and ultimately the ability to forecast solar flares – requires further analysis of how the magnetic field over an AR behaves during a solar flare event. Although the magnetic reconnection associated with solar flares occurs high in the solar atmosphere, because the capability of direct coronal magnetic field measurements does not exist, we rely on measurements of the photospheric magnetic field. However, photospheric – and even subphotospheric – motions drive the twisting and shearing of coronal magnetic structures.

The purpose of this study is to detect potential magnetic reconnection signatures associated with solar flare occurrence within the photospheric magnetic field, in order to better understand the underlying physics principles involved with such phenomenon. The work done here expands upon that of Whitney et al. (2020), the basis of which originated from a case study of the Labor Day 2017 storms performed by Loper (2018). Specifically, an analysis of photospheric magnetic field data during solar flare events was used to identify and compare the trends of differing flare classes for varying time intervals leading up to an event, as well as the trends of flares that occur with and without a precursor flare.

II. Background

2.1. Previous Research

Whitney (2020) performed an epoch analysis of full vector-field component data of the photospheric magnetic field during a six-hour window around solar flare events – two hours prior to flare occurrence, four hours after – in order to identify and compare trends in the different categories of flare strengths, as well as discern potential signatures of magnetic reconnection. The study utilized data from the Solar Dynamics Observatory (SDO) Helioseismic and Magnetic Imager (HMI) and Space Weather HMI Active Region Patches (SHARPs) for a near decade-long period from May 2010 through September 2019, and found that a rise in both size and flux levels of small and moderate flares indicates that ARs may still be growing in size and strength while producing flares, with the exception of X-class flares that showed opposite trends, suggesting that they have reached maximum size and strength. Additionally, the helicity and twist parameters showed greatest variability throughout the flare duration, and a sudden increase in these parameters following M- and X-class flares implies an increase in the complexity of the magnetic field configuration. Ultimately, for the purposes of solar flare forecasting, few of the magnetic parameters showed strong patterns or distinct signatures.

Mason and Hoeksema (2010) also performed an epoch analysis with a dataset of similar size to find statistical relationships between the solar magnetic field and flares, but their study utilized data from the SOHO/MDI. The data consisted of full-disk line-of-sight (LoS) magnetograms on a 96-minute cadence for 1075 ARs and over 6000 flares (B-class or greater) spanning the period from 15 April 1996 to 31 December 2008. Based on their

predictive success in previous studies, the magnetic parameters investigated were the total unsigned magnetic flux, primary inversion line (PIL) length, effective separation (i.e. the effective distance between the two bipolar regions of an AR), and gradient-weighted inversion-line length (GWILL). Results showed that of the four parameters, the GWILL was the most associated with flaring, but is still a poor predictor of flares in real-time. However, there is still hope yet as it was determined that a superposed epoch analysis does have the capability to pick out weak systematic responses indicating flare associated signatures.

Compared to Mason and Hoeksema (2010) and Whitney (2020), the majority of studies that utilize vector magnetic field data to investigate the relationship between the solar magnetic field and flare occurrence focus on smaller datasets and case studies. This is partially due to the fact that the HMI has only just recently been operational for a full decade. For example, Bobra and Couvidat (2015) attempted to forecast M- and X-class flares with a machine-learning algorithm using HMI vector magnetic field data. The catalog of data used to train the algorithm spanned from May 2010 to May 2014, and consisted of 303 positive examples – defined as an AR that flares within 24 hours after a sample time – and 5000 randomly selected negative examples – defined as an AR that does not flare within ±48 hours from the sample time. Results showed that the four magnetic parameters with the highest feature score (i.e. a measure of relevancy or how discriminative a parameter is) were the total unsigned current helicity, total magnitude of the Lorentz force, total photospheric magnetic free energy density, and total unsigned vertical current. Additionally, Bobra and Couvidat (2015) determined that the predictive capability of the

algorithm using only these four parameters was approximately the same as that of the top 13 parameters.

Kazachenko et al. (2017) compared the Geostationary Operational Environmental Satellite (GOES) peak X-ray flux with corresponding AR and flare ribbon – enhancements in Hα and 1600 Å emissions associated with the footprints of newly reconnected flux tubes on the solar surface – properties. Their database extended from April 2010 to April 2016 and consisted of 3137 solar flare events of magnitude C1.0 or stronger within 45° from the central meridian, observed by SDO. It was found that the peak X-ray flux was more strongly correlated with the flare ribbon reconnection flux, flare ribbon area, and the fraction of AR flux that undergoes reconnection than with the AR unsigned magnetic flux. This indicates that the strength of a solar flare is driven more by the magnetic flux associated with the reconnection specifically than the flux of the entire AR.

Leka and Barnes (2007) applied statistical tests based on linear discriminant analysis to 29 different photospheric magnetic parameters in order to identify flare producing properties of an AR. The data used in their study were University of Hawaii Imaging Vector Magnetograph daily magnetograms obtained between 2001 and 2004, comprising 496 numbered ARs. It was found that significant excess energy, large vertical currents, and considerable current helicity are associated with large ARs, as measured by the total flux. Additionally, the parameters with the highest correlation with flare production were totals of various quantities over the entire AR, complemented by measures of shear; the parameter most correlated was the total excess photospheric magnetic energy. Ultimately it was determined that no parameters made a strong distinction between flare producing and quiet ARs. However, Leka and Barnes (2007) noted that inclusion of the

evolution of the photospheric field or the coronal magnetic field could lead to better distinguishing of flare producing ARs.

In a study by Priest and Forbes (2002) it was determined that the time required for enough energy to build up in the magnetic field over an AR for a large flare to occur is approximately one day, whereas the time required for a moderate flare is only a couple hours. From this came one of the motives of the present study to compare the trends in magnetic parameters during varying time intervals leading up to a flare occurrence. The idea being that during the time of energy buildup (which increases with increasing flare strength) and flare occurrence, common trends in the magnetic parameters would be seen for the varying flare classes – i.e., the trends for X-class flares during a 24-hour interval would be roughly the same as those for M-class flares during a 12-hour interval, C-class flares during a six-hour interval, and B-class flares during a three-hour interval.

Another case study of the Labor Day 2017 storms performed by Verma (2018) investigated the morphological, magnetic, and horizontal flow properties associated with two specific X-class flares (X2.2 and X9.3) that occurred consecutively within the same AR on 6 September 2017. Utilizing continuum images, LOS and vector magnetograms, and 1600 Å UV images during a seven-hour time period around the flares, it was determined that the X2.2 flare acted as a precursor that set the stage for the stronger, more extended X9.3 flare. Specifically, flow patterns along the PIL that resulted from the X2.2 flare contributed to more strongly sheared magnetic field structures across the AR that led to the X9.3 flare. This idea of how the explosive motions of a flare can result in greater shearing and potential for loss of equilibrium over other portions of an AR, leading to a

stronger flare, was investigated further in the present study by comparing the trends of various magnetic parameters during flares that occur with and without a precursor.

Most of the studies that investigate the nature and effects of precursor flares are either case studies – looking at a few major flares with a couple precursors – or focus on the changes in an AR within a one-hour time interval before the major flare. Very few studies have looked at a more comprehensive and longer evolution of precursor activity leading up to major flares. One such study, performed by Gyenge et al. (2016), investigated the spatio-temporal distribution of precursor flares during a 24-hour interval preceding M- and X-class flares. The location of precursors could indicate the section of an AR where the magnetic field is progressively altered by successive reconnection events; the temporal distribution could reveal the characteristic time at which the destabilization of the field leading to a major event starts (Gyenge et al., 2016). The study considered only M- and X-class flares that were observed simultaneously by the GOES and Reuven Ramaty High Energy Solar Spectroscopic Imager (RHESSI) satellites, while the dataset for precursor flares came solely from RHESSI. With this, a total of 49 X-class flares (with 1001 associated precursors) and 315 M-class flares (with 3151 associated precursors) that occurred between 2002-2014 were examined. Gyenge et al. (2016) found that 18-24 hours prior to the major flare, the precursors of X-class flares followed a double peaked spatial distribution, while those of the M-class flares showed a lognormal distribution; however, six hours prior to the major flare, both classes showed the lognormal distribution. This supports the idea that the spatial extent of the reorganization of the magnetic field of an AR is larger for X-class flares than M-class flares. The temporal variation of precursors resembled a bell-shaped curve for both flare classes, with increased precursor activity

lasting 20-24 hours in both cases. Additionally, the aforementioned characteristic time was estimated to be approximately 12-15 hours before X-class flares and approximately 7-10 hours before M-class flares.

2.2. HMI Data

The HMI is a joint project between the Stanford University Hansen Experimental Physics Laboratory, the High Altitude Observatory (HAO), the Lockheed Martin Solar and Astrophysics Laboratory (LMSAL), and an additional 21 institutions, that is ultimately a part of National Aeronautics and Space Administration (NASA)'s Living With a Star (LWS) program (Scherrer et al., 2012). Since 1 May 2010, it has been operational onboard NASA's SDO, and is the first instrument to continuously map the photospheric vector magnetic field across the full solar disk from space with high cadence (Bobra et al., 2014). The intent of the HMI is to study the dynamics of the convection zone – the layer just below the photosphere – and the solar dynamo; the genesis and evolution of various solar activity features; connections between the Sun's internal processes and dynamics within the corona and heliosphere; sources and drivers of magnetic activity; and precursors of solar activity/disturbances to better space weather forecasting ability (Scherrer et al., 2012). For the most part, the instrument is based off of the highly successful MDI, with some significant improvements including the capability to observe full Stokes vector, full-disk filtergram data, two cameras instead of one, better temporal coverage and spatial resolution, and increased redundancy (Schou et al., 2012). HMI data can be obtained from the Joint Science Operations Center (JSOC) at Stanford University (JSOC, 2020b), and

greater detail regarding instrument description, calibration, and data handling can be found in Schou et al. (2012).

2.2.1. HARPs

Utilizing photospheric full-disk LoS magnetogram images produced on a 720 second (12 minute) cadence and continuum intensity images, an automated code identifies and tracks HMI Active Region Patches (HARPs) – i.e., an enduring, coherent magnetic structure whose size is on the scale of an AR (Hoeksema et al., 2014; JSOC, 2020a). HARP data files include both the HARP number and National Oceanic and Atmospheric Administration (NOAA) AR number, which may coincide as a single region or multiple NOAA ARs may be associated with a single HARP. Detailed steps on how HARPs are identified can be found in Hoeksema et al. (2014). There are two types of HARPs (JSOC, 2020c):

(1) Near-real time (NRT) HARPs, which are calculated as soon as possible and whose heliographic bounding box for the AR can change with each 12 minute time step

(2) Definitive HARPs, which are defined either after an AR has traversed the face of the solar disk or five days after the AR has decayed (whichever is first), and whose heliographic bounding box are constant over time.

Near real time HARP information is most useful for space weather forecasting; however, the need for rapid processing results in a loss of some of the convenient features of the definitive HARPs, such as constant size, known ancillary information like NOAA AR numbers, and inclusion of data before the first emergence of flux (JSOC, 2020c).

2.2.2. SHARPs

JSOC also produces the SHARP data series, which contains various space weather parameters/indices calculated from the photospheric vector magnetogram data of AR patches every 12 minutes; only data that are both above a high-confidence threshold and within a HARP contribute to the calculation of SHARP parameters (JSOC, 2020c; Bobra et al., 2014). The SHARP parameters, along with their descriptions and formulas, utilized in this study are summarized in Table 2. With further development of the SHARP database, additional parameters will become available, including models of the coronal field and characterizations of the magnetic-inversion lines (Bobra et al., 2014).

As with the HARP data series, there are definitive SHARPs – better calibrated and most complete data, with an approximately 35-day delay in availability – and NRT SHARPs – quick-look data, available within 3 hours. In addition to the difference in the HARP bounding box as described in the previous section, the input data for NRT and definitive SHARPs differ in completeness and calibration, with calibrations and corrections to the NRT data relying on predicted conditions (Bobra et al., 2014; Hoeksema et al., 2014). Furthermore, the annealing parameters for disambiguation are adjusted to enable faster computation for NRT processing (Bobra et al., 2014). Since the present study was focused on an analysis of magnetic parameters during flare events, as opposed to specifically forecasting flare occurrence, the definitive SHARP data series was used instead of the NRT series.

Table 2. SHARP parameters, descriptions, and calculations (From Whitney, 2020). All summations are over the total number of pixels, N.

Keyword	Description	Unit	Formula
AREA_ACR	De-projected area of active pixels	μH	$A_{total} = \sum dA$
USFLUX	Total unsigned flux	$Maxwells$	$\phi = \sum \lvert B_z \rvert dA$
MEANGAM	Mean inclination angle	$Degrees$	$\bar{\gamma} = \frac{1}{N} \sum \tan^{-1}\left(\frac{B_h}{B_z}\right)$
MEANGBT	Mean value of the total field gradient	G/Mm	$\overline{\lvert \nabla B_{tot} \rvert} = \frac{1}{N} \sum \sqrt{\left(\frac{\partial B}{\partial x}\right)^2 + \left(\frac{\partial B}{\partial y}\right)^2}$
MEANGBZ	Mean value of the vertical field gradient	G/Mm	$\overline{\lvert \nabla B_z \rvert} = \frac{1}{N} \sum \sqrt{\left(\frac{\partial B_z}{\partial x}\right)^2 + \left(\frac{\partial B_z}{\partial y}\right)^2}$
MEANGBH	Mean value of the horizontal field gradient	G/Mm	$\overline{\lvert \nabla B_h \rvert} = \frac{1}{N} \sum \sqrt{\left(\frac{\partial B_h}{\partial x}\right)^2 + \left(\frac{\partial B_h}{\partial y}\right)^2}$
MEANJZD	Mean vertical current density	mA/m^2	$J_z \propto \frac{1}{N} \sum \left(\frac{\partial B_y}{\partial x} - \frac{\partial B_x}{\partial y}\right)$
TOTUSJZ	Total unsigned vertical current	A	$J_{z_{total}} = \sum \lvert J_z \rvert dA$
MEANALP	Characteristic twist parameter, α	$1/Mm$	$\alpha_{total} \propto \frac{\sum J_z B_z}{\sum B_z^2}$
MEANJZH	Mean current helicity	G^2/m	$\bar{H}_c \propto \frac{1}{N} \sum B_z J_z$
TOTUSJH	Total unsigned current helicity	G^2/m	$H_{c_{total}} \propto \sum \lvert B_z J_z \rvert$
ABSNJZH	Absolute value of the net current helicity	G^2/m	$H_{c_{abs}} \propto \lvert \sum B_z J_z \rvert$
SAVNCPP	Sum of the absolute value of the net currents per polarity	A	$J_{z_{sum}} \propto \lvert \sum^{B_Z^+} J_z dA \rvert + \lvert \sum^{B_z^-} J_z dA \rvert$
MEANPOT	Mean photospheric excess magnetic energy density	erg/cm^3	$\bar{\rho} \propto \frac{1}{N} \sum (\vec{B}^{Obs} - \vec{B}^{Pot})^2$
TOTPOT	Total photospheric magnetic energy density	erg/cm	$\rho_{total} \propto \sum (\vec{B}^{Obs} - \vec{B}^{Pot})^2 dA$
MEANSHR	Mean shear angle	$Degrees$	$\bar{\Gamma} = \frac{1}{N} \sum \cos^{-1}\left(\frac{\vec{B}^{Obs} \cdot \vec{B}^{Pot}}{B^{Obs} B^{Pot}}\right)$
SHRGT45	Percentage of pixels with a mean shear angle greater than 45°	$Percent$	$\frac{area\ with\ shear > 45°}{HARP\ area}$

2.3. Flare Data/Statistics

The Geostationary Operational Environmental Satellite (GOES) utilizes a detection algorithm to automatically identify various solar events, including solar flares. By comparing current data to three minutes' worth of previous observations, the algorithm can calculate the slope of the x-ray flux and determine the beginning, maximum, and end times of the solar events (SWPC, 2009). NOAA's Space Weather Prediction Center (SWPC) maintains an archive of all solar events and associated data, dating back to 1966 (SWPC, 2019).

The present study utilizes the same dataset retrieved from SWPC by Whitney (2020), with solar flare event and HMI data spanning from May 2010 to September 2019. The reason this same dataset was used is that solar activity was relatively low following September 2019, with only 38 B-class flares, three C-class flares, one M-class flares, and zero X-class flares occurring from October 2019 to September 2020. Statistically, the inclusion of these flares would have a negligible effect on the results of the study, thus it was easier to utilize the dataset that was already in a ready-to-use format. Further detail on the retrieval and formatting of the dataset can be found in sections 2.3 and 3.2 of Whitney (2020). Of note, the solar flare times are in Coordinated Universal Time (UTC), while SHARP data is in International Atomic Time (TAI); UTC and TAI only differ by 37 seconds (approximately 5% of the HMI observation cadence), thus the difference in time scales can be ignored (Whitney, 2020).

The total number of solar flares within the dataset was 13,507, the overwhelming majority of which were lower class flares (B- and C-class). A detailed breakdown of the

number of flares of each class and the occurrence of a precursor within a given time interval is provided in Table 3. It should be noted that A-class flares were not included in the analysis performed due to their minimal effects, as well as the fact that they are often washed out by the background x-ray flux. This washing out can also occur for lower magnitude B-class flares during solar max or periods with a high frequency of flares when the background x-ray flux is elevated, thus the total number of B-class flares in Table 3 is likely not the actual number that occurred during the time period considered (Whitney, 2020).

For the purposes of this study, a precursor flare was defined as a flare that occurs within the same AR and a given timeframe prior to a flare of equal or larger magnitude. A flare without a precursor was defined as one that had no other flare occur within the given timeframe prior to occurrence. With this, the analysis of flares with and without precursors did not include flares that occurred following a flare of larger magnitude within a given timeframe. Thus, the percentages of flares with and without precursors for each time interval in Table 3 do not necessarily add up to 100. A greater number of such cases occurred within the longer time intervals, leading to a drop in the combined percentage of flares with and without a precursor for increasing time intervals (Table 3). This percentage drop is greater for lower magnitude flares than larger magnitude; X-class flares had no percentage drop with increasing time interval, while B-class flares had the greatest percentage drop.

The temporal distribution of precursor flares within a 24-hour interval for each flare class can be seen in Figure 2. The B-, C-, and M-class flares all show a general increase in precursor activity over the 24 hours preceding occurrence. As would be expected, the B-

and C-class flares show the most significant increase in precursor activity starting approximately six to eight hours prior to occurrence. This is due to the fact that more often than not a B- or C-class flare is not the dominant flare for an extended period of time. Precursor activity ahead of M-class flares start to significantly increase approximately 8-12 hours prior to occurrence, similar to what Gyenge et al. (2016) found.

Table 3. Distribution of flare classes in the dataset.

Flare Class	A	B	C	M	X	Total
Number Overall	61	5493	7210	697	46	13507
Percentage Overall	0.45%	40.67%	53.38%	5.16%	0.34%	100%
Percentage of flare class with a Precursor within a 3-hour interval	0%	12.87%	22.16%	49.79%	54.35%	19.82%
Percentage of flare class without a Precursor within a 3-hour interval	8.20%	48.46%	49.97%	40.32%	41.30%	48.64%
Percentage of flare class with a Precursor within a 6-hour interval	0%	16.75%	29.10%	62.98%	67.39%	25.82%
Percentage of flare class without a Precursor within a 6-hour interval	8.20%	37.41%	36.27%	24.10%	28.26%	35.95%
Percentage of flare class with a Precursor within a 12-hour interval	0%	20.15%	35.10%	72.02%	82.61%	30.93%
Percentage of flare class without a Precursor within a 12-hour interval	8.20%	27.49%	24.79%	14.06%	13.04%	25.22%
Percentage of flare class with a Precursor within a 24-hour interval	0%	23.03%	39.68%	77.04%	89.13%	34.83%
Percentage of flare class without a Precursor within a 24-hour interval	4.92%	19.28%	16.64%	8.47%	6.52%	17.21%

Very different to the other flare classes, as well as the findings of Gyenge et al. (2016), precursor activity ahead of the X-class flares showed no obvious trend, with activity fluctuating throughout the 24 hours. The difference between the X-class flare

precursor activity in Figure 2 and the results of Gyenge et al. (2016) – which is the similar increasing trend seen with the other classes – could be the result of different data collection. The present study utilized GOES flare data solely, whereas Gyenge et al. (2016) utilized GOES data for the "major" flares and RHESSI data for the associated precursors, which is more sensitive to the smaller magnitude flares and microflares. Thus, while there were only 269 associated precursors within a 24-hour interval ahead of the 46 X-class flares in this study, there were 1001 precursors ahead of the 49 X-class flares in Gyenge et al. (2016). Additionally, missing data for the NOAA AR number within the GOES dataset used in the present study (see Methodology) resulted in 62 potential precursors for X-class flares not being considered – a decent amount relative to the 269 confirmed precursors. Of these 62 potential precursors, 38 (or approximately 61%) occurred within a 12-hour interval ahead of the X-class flares.

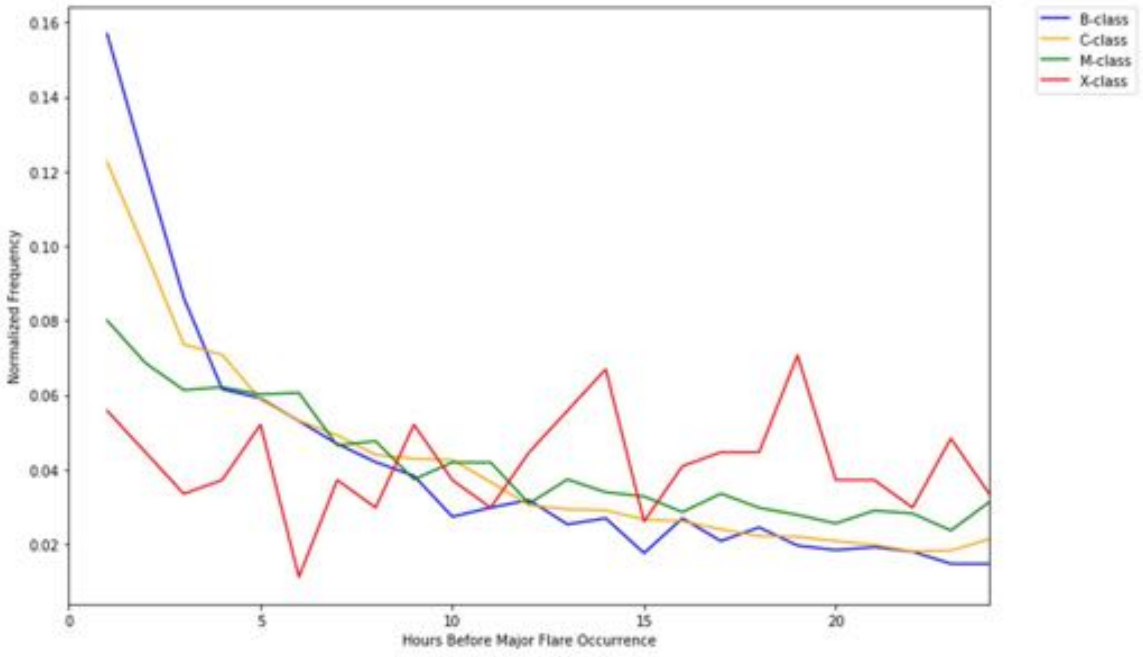

Figure 2. Temporal distribution of precursor flares.

III. Methodology

As previously mentioned, the dataset used in this study was the same as that used by Whitney et al. (2020), which included nearly all of Solar Cycle 24. The dataset consisted of solar flare event data from SWPC (start time, max time, end time, flare class/magnitude, and NOAA AR number) and HMI data from JSOC (date/time, longitude, HARP number, associated NOAA AR number, and all SHARP parameters), for the time period of 1 May 2010 to 4 September 2019. Connection of the solar flare event data and HMI data was established by associating the start time of each flare to the nearest HARP data time. Flare start times were used instead of flare max times because (1) the data collected would be affected by the occurrence and progression of the flare at max time, and (2) the time between the flare start and maximum is not constant, making it impossible to label the data prior to the flare max as part of the flare itself or part of the buildup (Whitney et al., 2020).

3.1. Data Filters

Only flares with an associated NOAA AR were considered in this study since a precursor flare was defined as a flare that occurs within the same AR and a given timeframe prior to a flare of equal or larger magnitude. This meant nearly 16% of the dataset (2,085 out of the total 13,507 flares) was filtered out. Additionally, flares that occurred at longitudes greater than ±70° were filtered out to avoid data affected by solar limb effects and/or from incomplete HARPs as they rotate onto and off the solar disk. As a result of the optical depth of the plasma in the solar atmosphere and the geometry of the LoS, satellites survey only the upper reaches of the photosphere near the solar limb, while surveying the

base of the photosphere near the center of the solar disk. This, along with a decrease in temperature with height in the photosphere, leads to the limb darkening that can be seen in solar imagery (see Figure 3). Furthermore, for features near the solar limb the LoS looks across instead of direct, which leads to the LoS magnetic fields measured by the HMI to be predominantly horizontal rather than radial (Whitney et al., 2020).

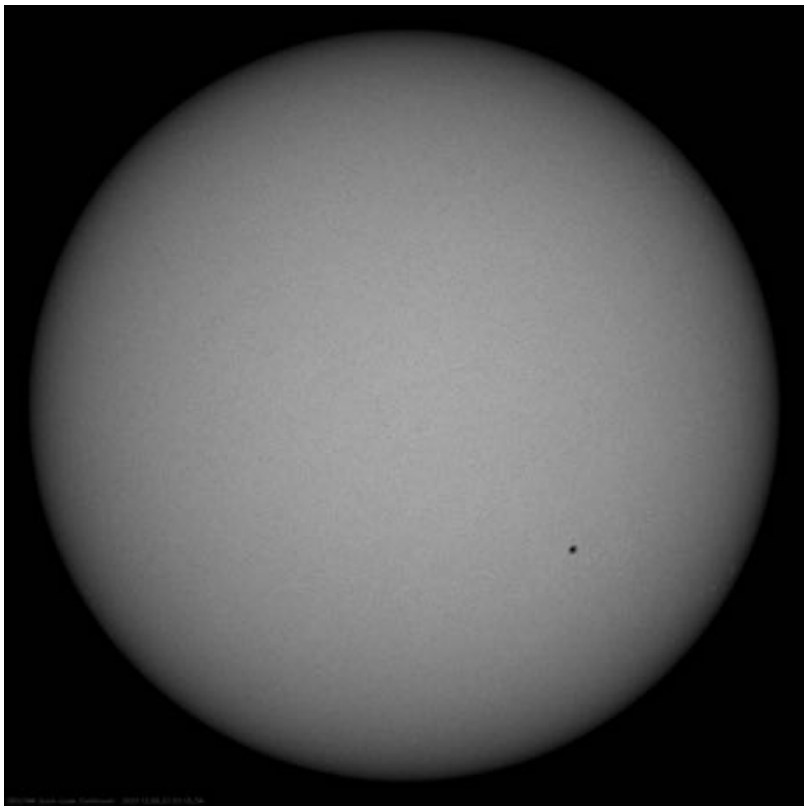

Figure 3. SDO/HMI Intensitygram from 9 Dec 2020 (retrieved from JSOC, 2020b).

A longitude of ±70° was chosen as the threshold for this study in part because beyond 70° the signal-to-noise ratio in the SHARP parameters significantly increases (Bobra et al., 2014). In addition, Whitney et al. (2020) found no significant differences between a 70° threshold and a 45° threshold – used in other studies such as Kazachenko et

al. (2014) to eliminate data that is primarily transverse instead of radial. Data plotted with the two different thresholds showed fluctuations within a few percent, indicating that "the SHARP calculations do make corrections for longitude in the Stokes parameters" (Whitney et al., 2020).

To investigate the potential time dependence of the trends in magnetic parameters for varying flare classes, data for the following time intervals around each solar flare occurrence was used in the analysis:

- 3-hour interval, defined as 3 hours before occurrence through 6 hours after
- 6-hour interval, defined as 6 hours before occurrence through 6 hours after
- 12-hour interval, defined as 12 hours before occurrence through 6 hours after
- 24-hour interval, defined as 24 hours before occurrence through 6 hours after.

To ensure data would not overlap, flares that occurred within the different epoch intervals of each other were filtered out, with the largest magnitude flare remaining. The larger flares were kept due to the overwhelming number of smaller flares in the dataset, thus representation of flare classes/magnitudes would be slightly more balanced. Additional filtering was done to separate solar flare events based on precursor occurrence, in order to compare the trends in magnetic parameters for flares with and without a precursor flare.

With the data filters applied, 12 different subsets of data were analyzed. For each of the epoch intervals listed above, there were three separate subsets:

1. General subset, which consisted of all categories of flares – i.e. flares with a precursor, flares without a precursor, and flares that occurred after a larger magnitude flare

2. Precursor subset, which consisted only of flares that had a precursor flare occur within the given timeframe leading up to occurrence
3. No precursor subset, which consisted only of flares that had no other flare occur within the given timeframe leading up to occurrence.

3.2. Analysis

As indicated earlier, flare occurrence was defined by the flare start time as retrieved from the SWPC archive (SWPC, 2019). For each flare within a particular subset, the start time was associated with the nearest HARP data time, and from that, all HMI data within the particular epoch interval of the subset was gathered. For example, for a flare in one of the 3-hour interval subsets, all HMI data within three hours before the HARP data time nearest the flare start time through six hours after that time was gathered. Given the SDO/HMI 12-minute cadence for data collection, this meant that for each flare in a 3-hour interval subset there were 45 data points; for each flare in a 6-hour interval subset there were 60 data points; for each flare in a 12-hour interval subset there were 90 data points; and for each flare in a 24-hour interval subset there were 150 data points. To effectively compare the solar flare events and changes relative to flare occurrence, all SHARP parameters gathered for a particular flare were normalized to the value at the flare's start time. Additionally, within each subset, the averages of each parameter for each flare class and magnitude at every time step were calculated.

Once all data had been gathered and normalized for each flare in the different subsets, a mask was applied to each subset to remove outliers. An outlier was defined as a flare that had any parameter with a value greater than three standard deviations from the

average value at any time within the particular epoch interval. The normalized standard deviation limits for each parameter and data subset can be found in Appendix A. Removal of outliers was necessary to accurately analyze the trends of the magnetic parameters during solar flare events, as results were highly skewed when these flares were included. Following the removal of outliers, the averages were recalculated. With the data filters and outlier removal masks applied, the number of flares considered in the analysis for each subset are displayed in Tables 4, 5, and 6.

For plotting purposes, time arrays for each epoch interval were created with all flares set to start at an arbitrary time of 12:00. This ensured all flare occurrences lined up and SHARP parameters converged to a value of 1.00 at 12:00, allowing for trends prior to and following flare occurrence to be more easily discernable. Just as Whitney et al. (2020) found, because of the sizeable amount of flares within the different subsets, when all were presented on a single plot, the plots became overcrowded and trends were difficult to determine. For this reason, the data subsets were summarized by plotting the flare averages instead.

3.3. Limitations

Given the vast amount of data involved – 13,507 solar flares and 2,669,718 HMI data points – there was, of course, missing data within the SWPC and HMI datasets. Specifically, across all the SHARP parameters, the average number of data points with missing values was 20,765, with a maximum number of 35,378. As mentioned before, nearly 16% of the solar flares had missing NOAA AR numbers.

Though the HMI is highly beneficial, being the first instrument to continuously map the photospheric vector magnetic field across the full solar disk (Bobra et al., 2014), its 12-minute cadence between observations does bring about some limitations. First off, for time scales less than 12 minutes, any changes in the photospheric magnetic field are lost. Furthermore, if a flare occurs during the time between observations, "flare times may be incorrect by as many as six minutes, [and] the nearest observation time may be after the start time of the flare, thus resulting in…contamination of the data due to the ongoing flare" (Whitney et al., 2020).

Lastly, as noted in other studies, photospheric magnetic field data may not be sufficient enough to fully understand the physics involved with magnetic reconnection since reconnection takes place higher in the solar atmosphere. Though the photospheric and chromospheric/coronal magnetic fields may be connected, direct measurements of the chromospheric and coronal magnetic fields would be able to provide a fuller depiction of magnetic reconnection. Moreover, the opacity of the solar atmosphere can be altered during a flare event, affecting the accuracy of the photospheric observations during and immediately following the event (Whitney et al., 2020).

Table 4. Distribution of flare classes in the General subsets following data filters & outlier removal (Adapted from Whitney, 2020).

Epoch Interval	Flare Class	Number of Flares Considered	Comparison to Total Considered in Epoch Interval	Comparison to Class Total in Full Dataset (Table 3, Column 2)
3-hour	B	1373	35.214 %	24.995 %
	C	2116	54.270 %	29.348 %
	M	379	9.720 %	54.375 %
	X	31	0.796 %	67.739 %
	Total	3899	100 %	28.867 %
6-hour	B	865	34.353 %	15.747 %
	C	1305	51.827 %	18.100 %
	M	318	12.629 %	45.624 %
	X	30	1.191 %	65.217 %
	Total	2518	100 %	18.642 %
12-hour	B	452	30.706 %	8.229 %
	C	763	51.834 %	10.583 %
	M	228	15.489 %	32.712 %
	X	29	1.971 %	63.043 %
	Total	1472	100 %	10.898 %
24-hour	B	211	26.675 %	3.841 %
	C	388	49.052 %	5.381 %
	M	168	21.239 %	24.103 %
	X	24	3.034 %	52.174 %
	Total	791	100 %	5.856 %

Table 5. Distribution of flare classes in the Precursor subsets following data filters & outlier removal (Adapted from Whitney, 2020).

Epoch Interval	Flare Class	Number of Flares Considered	Comparison to Total Considered in Epoch Interval	Comparison to Class Total in Full Dataset (Table 3, Column 2)	Comparison to Class Total with a Precursor (Table 3, Column 3/5/7/9)
3-hour	B	295	23.338 %	5.370 %	41.726 %
	C	736	58.228 %	10.208 %	46.058 %
	M	216	17.089 %	30.990 %	62.248 %
	X	17	1.345 %	36.957 %	68.000 %
	Total	1264	100 %	9.358 %	47.217 %
6-hour	B	287	23.448 %	5.225 %	31.196 %
	C	685	55.964 %	9.500 %	32.650 %
	M	231	18.872 %	33.142 %	52.620 %
	X	21	1.716 %	45.652 %	67.742 %
	Total	1224	100 %	9.062 %	35.092 %
12-hour	B	210	21.538 %	3.823 %	18.970 %
	C	545	55.897 %	7.559 %	21.533 %
	M	199	20.410 %	28.551 %	39.641 %
	X	21	2.155 %	45.652 %	55.263 %
	Total	975	100 %	7.219 %	23.337 %
24-hour	B	122	19.709 %	2.221 %	9.644 %
	C	323	52.181 %	4.480 %	11.290 %
	M	153	24.717 %	21.951 %	28.492 %
	X	21	3.393 %	45.652 %	51.220 %
	Total	619	100 %	4.583 %	13.159 %

Table 6. Distribution of flare classes in the Non-Precursor subsets following data filters & outlier removal (Adapted from Whitney, 2020).

Epoch Interval	Flare Class	Number of Flares Considered	Comparison to Total Considered in Epoch Interval	Comparison to Class Total in Full Dataset (Table 3, Column 2)	Comparison to Class Total without a Precursor (Table 3, Column 4/6/8/10)
3-hour	B	1699	39.084 %	30.930 %	63.824 %
	C	2455	56.476 %	34.050 %	68.138 %
	M	178	4.095 %	25.538 %	63.345 %
	X	15	0.345 %	32.609 %	78.947 %
	Total	4347	100 %	32.183 %	66.164 %
6-hour	B	1199	40.330 %	21.828 %	58.345 %
	C	1665	56.004 %	23.093 %	63.671 %
	M	100	3.364 %	14.347 %	59.524 %
	X	9	0.302 %	19.565 %	69.231 %
	Total	2973	100 %	22.011 %	61.223 %
12-hour	B	788	41.715 %	14.346 %	52.185 %
	C	1052	55.691 %	14.591 %	58.870 %
	M	44	2.329 %	6.313 %	44.898 %
	X	5	0.265 %	10.870 %	83.333 %
	Total	1889	100 %	13.985 %	55.461 %
24-hour	B	469	42.405 %	8.538 %	44.287 %
	C	613	55.425 %	8.502 %	51.083 %
	M	22	1.989 %	3.156 %	37.288 %
	X	2	0.181 %	4.348 %	66.667 %
	Total	1106	100 %	8.188 %	47.590 %

IV. Results and Discussion

The limited number of X-class flares – a consequence of the nature of extreme events – resulted in greater variability in the data for that flare class. As a result of this greater variance, the trends for smaller flares are not as readily discernable. Therefore, all figures in this section were reproduced without the X-class flare data (see Appendix B). Though it was more often the case for the X-class flares, ultimately for all flare classes some of the SHARP data was sporadic, with no distinguishable trends. With this, the trends/behavior of the magnetic parameters analyzed and discussed in this section focuses only on those that were more consistent and discernable. Additionally, as noted in Table 6, the 24-hour Non-Precursor subset consisted of only two X-class flares – comprising of only one flare sub-classification (X1.0) – considered for the analysis, which led to extreme variability in the data and no discernible trends. Thus, comparison of Precursor and Non-Precursor subsets is discussed only for the 3-, 6-, and 12-hour epoch intervals; the 24-hour epoch interval is only included in the discussion of the General subsets.

The epoch analyses of the flare averages for the General subsets (Figures 4-7) can be found in section 4.1, where the potential time dependence with varying flare strength is discussed. The epoch analyses of the flare averages for the Precursor and Non-Precursor subsets (Table 7 and Figures 8-13) can be found in section 4.2, where the trends of SHARP parameters for flares with and without a precursor(s) are compared. Within the plots, flare occurrence (or start time) is represented by the vertical dashed line. The colored lines represent the average values of the different flare classes, while the thick, dashed line represents the average values of all flares within the subset.

4.1. General Subsets

Comparison of the General subsets for all time intervals identified (1) the broader differences and (2) the potential time dependence of magnetic conditions leading up to and during flare events of different strengths. Regarding (1), X-class flares showed dissimilar/opposite trends than the B-, C-, and M-class flares for the following parameters:

- LoS Area of Active Pixels
- Total Unsigned Flux
- Mean Vertical Current Helicity
- Characteristic Twist Parameter.

For the LoS Area of Active Pixels – a measure of AR size – the B-, C-, and M-class flares all show an increase before and after flare occurrence for all time intervals; X-class flares show a decrease before occurrence for the 3-, 6-, and 12-hour intervals, and after occurrence for all time intervals. This is likely because an AR has reached maximum growth by the time an X class flare is released, whereas the AR may continue to grow even after smaller class flares occur. Though it will be discussed further in Section 4.2, it should be noted that X-class flares with precursors show a similar increasing trend in LoS Area of Active Pixels that the other flare classes show, but the non-precursor cases show the decreasing trend and dominate the data for this parameter. Compared to the more consistent increase in Total Unsigned Flux both prior to and immediately following flare occurrence that the other flare classes show, X-class flares have much greater fluctuation in the parameter and often show an initial decrease after flare occurrence. This further suggests that an AR may be reaching maximum growth around the occurrence of an X-class flare.

For the Mean Vertical Current Helicity and Characteristic Twist Parameter, X-class flares show a large spike/increase immediately following occurrence that the other classes do not show, as well as a decreasing trend 12 hours prior to occurrence, while the other classes don't show any significant trend. This could be the result of X-class flares having much greater polarity in magnetic field direction prior to reconnection. As the field lines become more and more oppositely directly – specifically in the vertical direction – the vertical components of the magnetic field (B_z) and current (J_z), from which the parameters are calculated, decrease since the field lines are fighting each other. Following reconnection and flare occurrence, that fighting ceases and the lines are directed in the same direction, so the parameters increase. Since the smaller class flares don't require the same degree of polarity, the intense fluctuation seen for X-class flares doesn't occur.

Concerning (2), none of the SHARP parameters showed a significant time dependence for varying flare strengths. The Absolute Value of the Net Vertical Current Helicity did show a decreasing trend in all time intervals prior to flare occurrence for the B- and C-class flares; in the 6-, 12-, and 24-hour intervals for the M-class flares; and in the 12- and 24-hour intervals for the X-class flares. However, there was no concrete example of time dependence in the sense of smaller magnitude flares (B- and C-class) having a particular trend solely at the shorter time intervals (3- and 6-hour) that the larger magnitude flares (M- and X-class) had solely at the longer time intervals (12- and 24-hour) as hypothesized. A possible explanation for this result is how much of the total energy built up within an AR is actually released by magnetic reconnection during a solar flare event. An AR that has been growing and evolving for a long period of time, such that enough energy for an X-class flare has built up within the magnetic field, may only produce a B-

class flare when reconnection occurs depending on the particular configuration of the field or possibly the energy density distribution of the field over the AR.

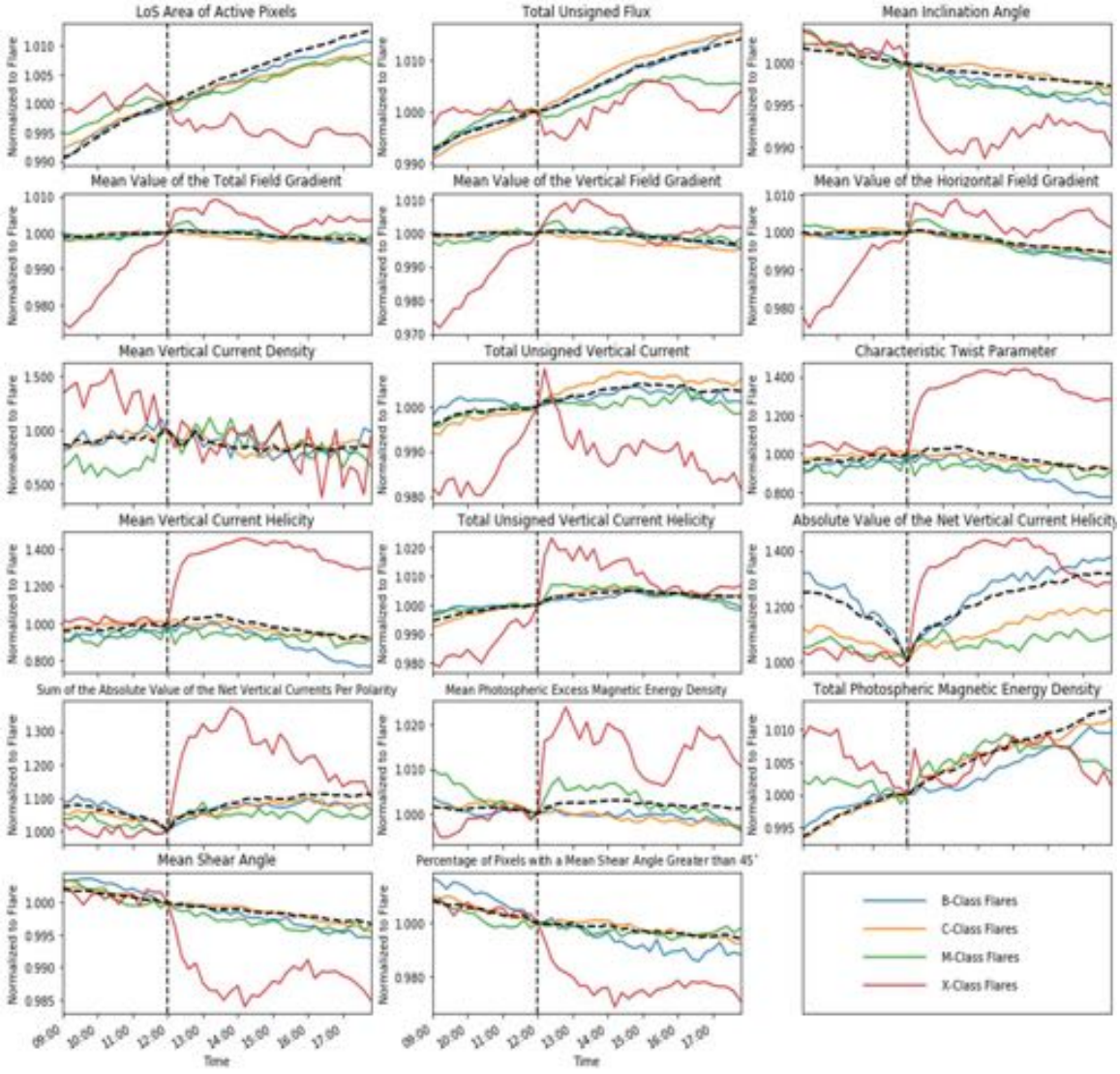

Figure 4. Epoch analysis for the 3-hour General subset of flares. All data are normalized to the values at the start time of the flares. The plots display the averages for all events in the associated flare class. Flares outside of three standard deviations from the average and outside of 70° heliographic longitude are excluded. SHARP data are acquired from JSOC using the Python notebook created by Glogowski and Bobra (2016) and flare start times are identified by SWPC (2019).

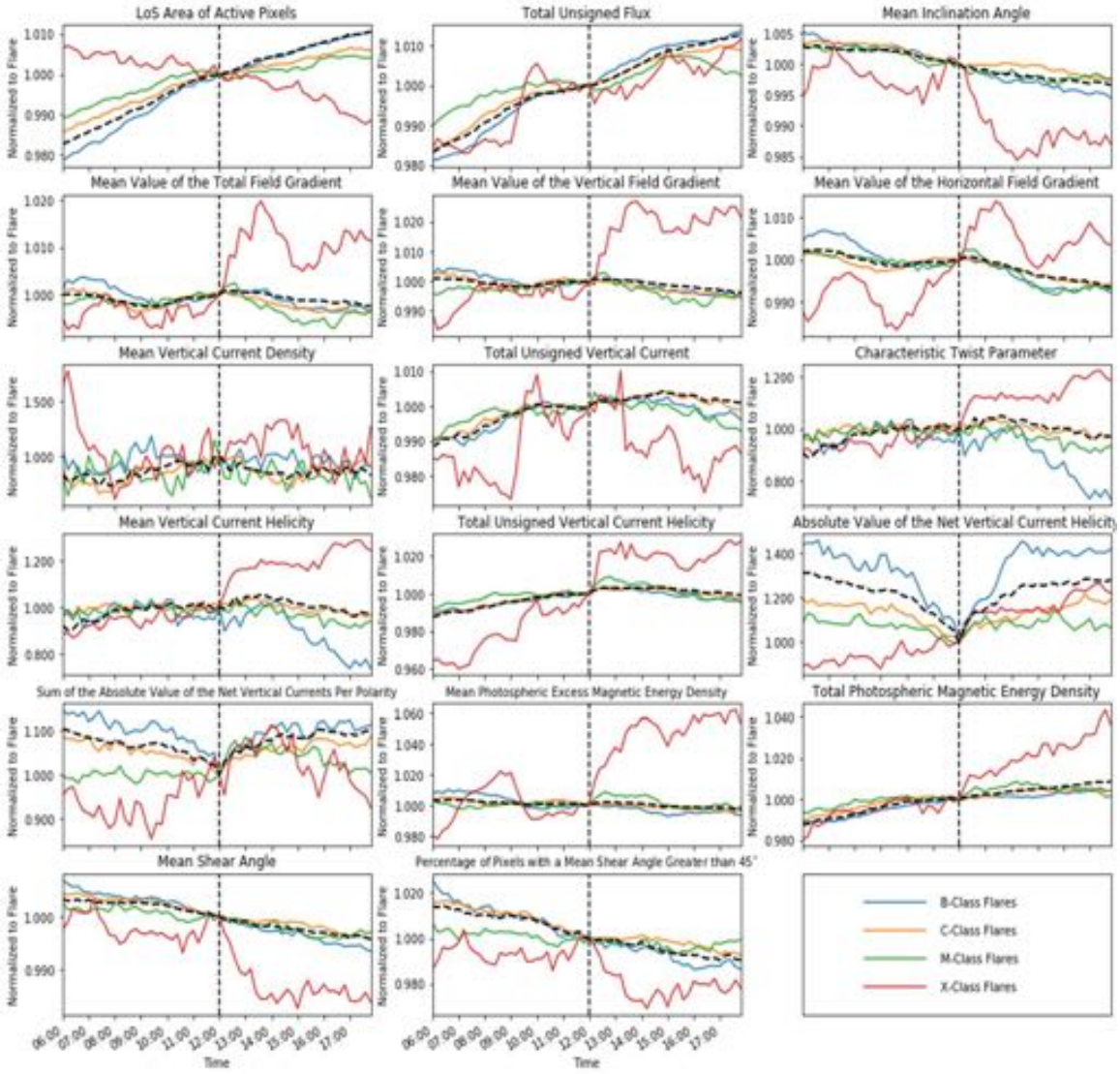

Figure 5. Epoch analysis for the 6-hour General subset of flares. All data are normalized to the values at the start time of the flares. The plots display the averages for all events in the associated flare class. Flares outside of three standard deviations from the average and outside of 70° heliographic longitude are excluded. SHARP data are acquired from JSOC using the Python notebook created by Glogowski and Bobra (2016) and flare start times are identified by SWPC (2019).

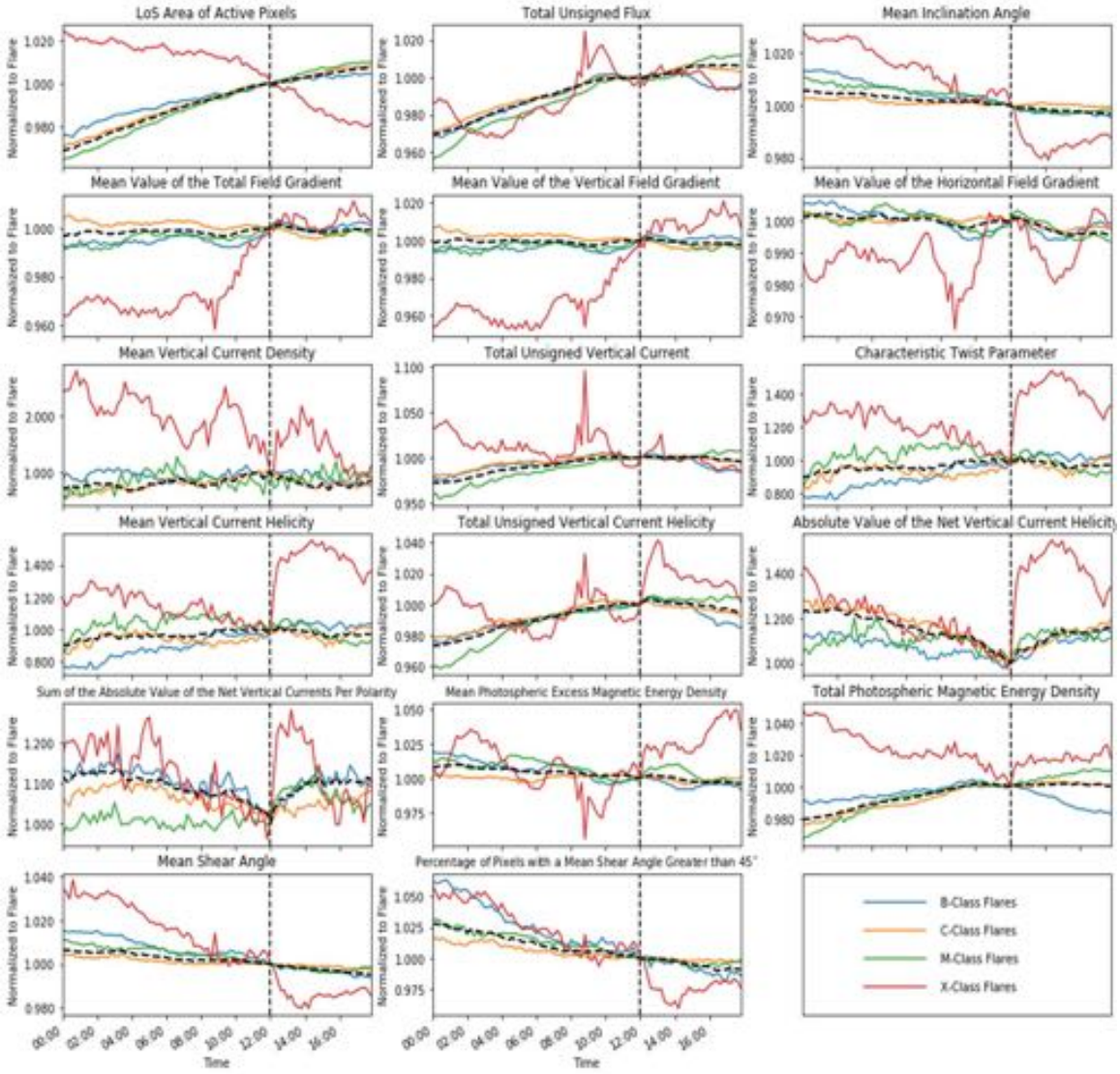

Figure 6. Epoch analysis for the 12-hour General subset of flares. All data are normalized to the values at the start time of the flares. The plots display the averages for all events in the associated flare class. Flares outside of three standard deviations from the average and outside of 70° heliographic longitude are excluded. SHARP data are acquired from JSOC using the Python notebook created by Glogowski and Bobra (2016) and flare start times are identified by SWPC (2019).

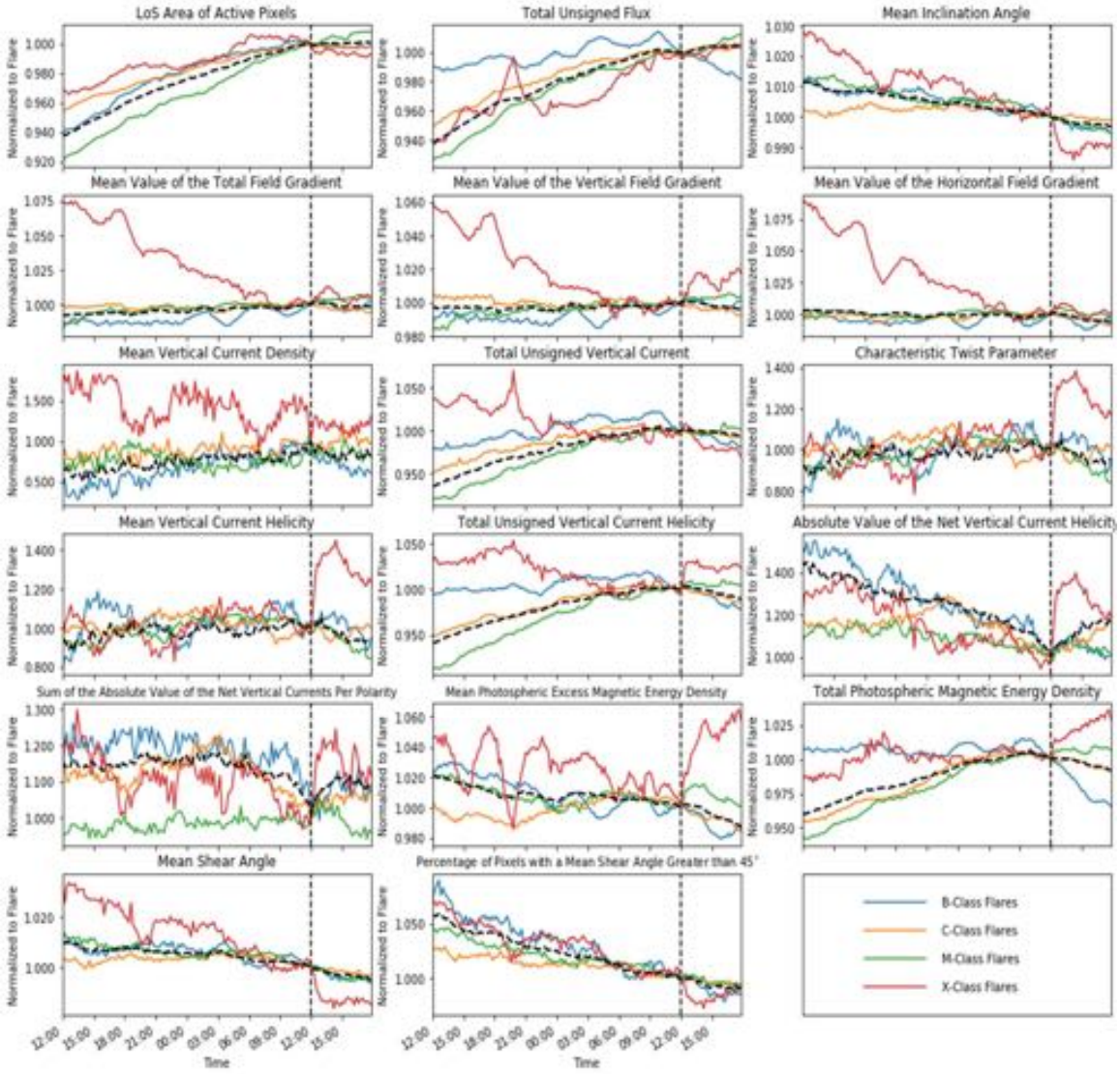

Figure 7. Epoch analysis for the 24-hour General subset of flares. All data are normalized to the values at the start time of the flares. The plots display the averages for all events in the associated flare class. Flares outside of three standard deviations from the average and outside of 70° heliographic longitude are excluded. SHARP data are acquired from JSOC using the Python notebook created by Glogowski and Bobra (2016) and flare start times are identified by SWPC (2019).

4.2. Precursor vs. Non-Precursor Subsets

Table 7 summarizes the SHARP parameters that showed dissimilar/opposite trends between flares with and without a precursor(s) for varying flare classes and time intervals. In general, the differences in magnetic parameters of an AR between solar flare events that occur with a precursor(s) and those that occur without appear to be greater for X-class flares than the lower magnitude flares. Additionally, for X-class events, the differences are greater within the 3- and 6-hour epoch intervals than the 12-hour interval. The number and extent of dissimilar/opposite trends in the SHARP parameters for X-class flares with and without a precursor(s) drops from the 6-hour interval to the 12-hour interval. This suggests that the effect to which a precursor adjusts the magnetic conditions of an AR for a large flare event to occur drops in significance following a six-hour period between precursor and main flare occurrence.

Across the three epoch intervals investigated for the Precursor and Non-Precursor subsets, the following parameters were the most common in showing differences in the trends leading up to and following solar flare events:

- LoS Area of Active Pixels
- Total Unsigned Flux
- Mean Photospheric Excess Magnetic Energy Density
- Total Photospheric Magnetic Energy Density
- Total Unsigned Vertical Current Helicity
- Mean Shear Angle
- Percentage of Pixels with a Mean Shear Angle Greater than 45°.

The first four parameters listed above all showed more continuous increase prior to and following flare occurrence for flares that had a precursor(s), while those without showed leveling off or a decreasing trend. This behavior is more clear and concrete with X-class flares, relating back to the idea of maximum AR growth presented in section 4.1. The data suggests that ARs that have an X-class flare occur with no precursor may have reached maximum growth, with a significant portion of the energy associated lost by the flare, while those that produce X-class flares with a precursor(s) could still be growing and evolving. The fact that the averaged data for X-class flares with precursors still showed an increasing trend in these parameters following occurrence supports the idea that a X-class flare could be a precursor for a larger X-class flare (Verma, 2018).

Of particular interest with the Total Photospheric Magnetic Energy Density, across all time intervals the X-class flares that occurred without a precursor showed a sudden dip to a relative minimum approximately one hour prior to flare occurrence, while those with a precursor(s) showed continuous increase. Keeping in mind of course that at most only fifteen X-class flares were considered in the Non-Precursor subsets and one event with data substantially lower than the average at that one-hour prior mark could cause the dip that is seen, it is worth noting the feature as a potential signature for forecasting purposes. As more X-class events occur in the future, if the feature continues to be seen across a more statistically significant amount data, the sudden dip in Total Photospheric Magnetic Energy Density may prove to be an indicator for an X-class flare that occurs without a precursor.

Table 7. Summary of dissimilar/opposite trends in SHARP parameters between solar flares with and without a precursor(s) for varying flare class and time intervals. A cell with an 'x' means that particular parameter had a dissimilar trend for the specified flare class and time interval.

	3-hour				6-hour				12-hour			
Parameter	**B**	**C**	**M**	**X**	**B**	**C**	**M**	**X**	**B**	**C**	**M**	**X**
Los Area of Active Pixels				×				×			×	
Total Unsigned Flux		×	×	×		×	×	×			×	×
Mean Inclination Angle												
Mean Value of the Total Field Gradient												
Mean Value of the Vertical Field Gradient												
Mean Value of the Horizontal Field Gradient												
Mean Vertical Current Density												
Total Unsigned Vertical Current											×	
Characteristic Twist Parameter								×				
Mean Vertical Current Helicity								×				
Total Unsigned Vertical Current Helicity				×				×			×	×
Absolute Value of the Net Vertical Current Helicity								×				
Sum of the Absolute Value of the Net Vertical Currents Per Polarity												
Mean Photospheric Excess Energy Density	×	×		×		×		×		×		×
Total Photospheric Magnetic Energy Density		×	×	×	×	×	×	×		×	×	
Mean Shear Angle	×	×	×	×	×	×	×	×	×	×	×	
Percentage of Pixels with a Mean Shear Angle > 45°	×	×		×	×	×	×	×	×	×		

In regards to the Total Unsigned Vertical Current Helicity, across all time intervals the X-class flares that occurred with a precursor(s) showed a leveling off/continued increase following an initial spike after occurrence, whereas those without a precursor showed a decreasing trend following the initial spike after occurrence. This behavior is also likely connected to the concept of AR growth and evolution previously discussed. For X-class flares that occurred with a precursor(s), the Total Unsigned Vertical Current Helicity remains elevated or continues to increase following occurrence because the AR is still evolving and the magnetic field is continuing to become more and more complex. For X-class flares without a precursor, following the explosive motions of the flare that create the initial spike, the magnetic field begins to unravel and the AR starts to decay.

Lastly, for the shear related parameters, all flare classes at all time intervals – with the exception of X-class flares at the 12-hour epoch interval – showed more significant decreasing in shear before and after flare occurrence for flares without a precursor(s), while those with often leveled out and even increased. This suggests that precursors do, in fact, enhance the shear over an AR, helping set up the conditions for magnetic reconnection necessary for the occurrence of a larger flare.

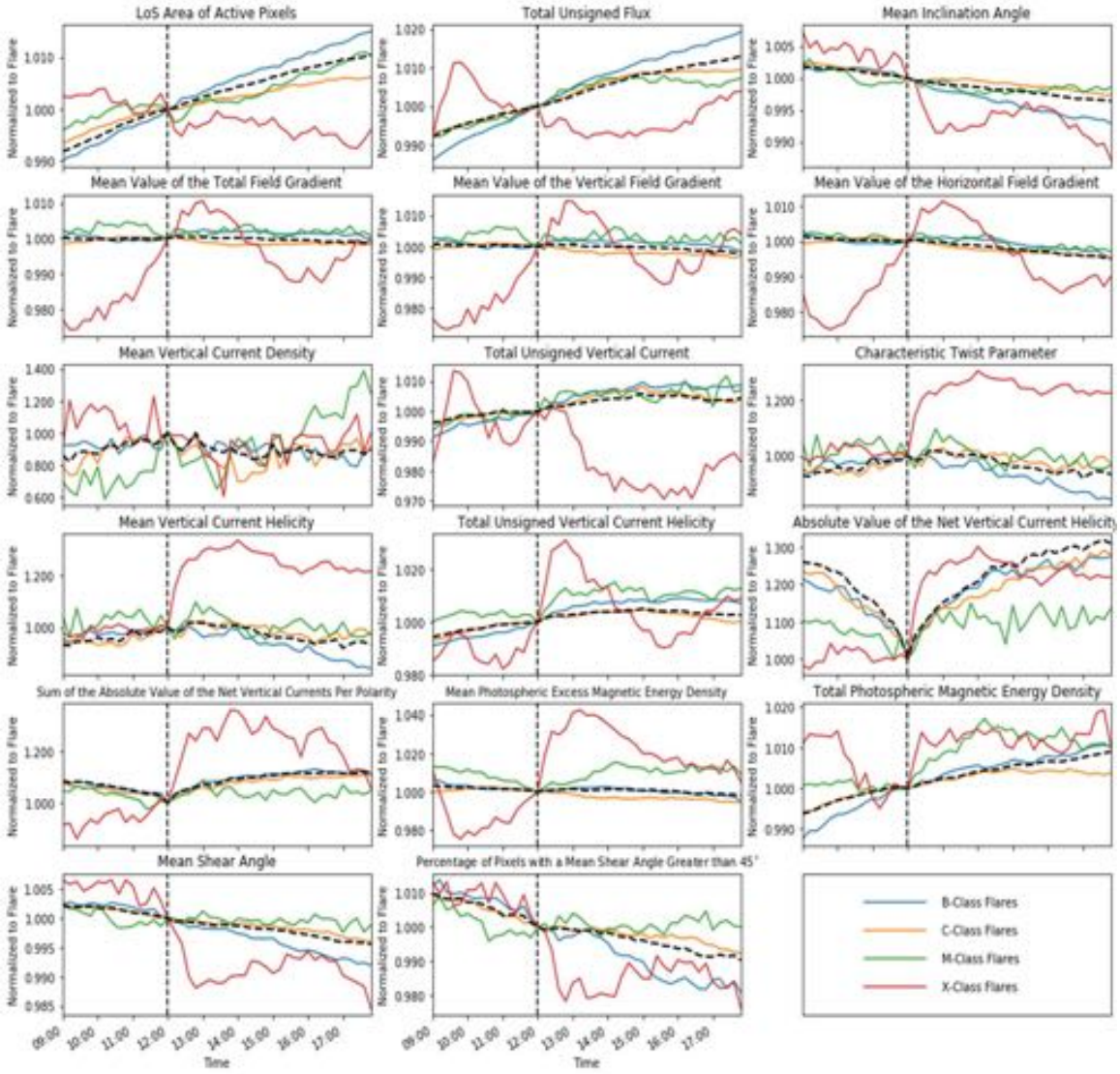

Figure 8. Epoch analysis for the 3-hour Non-Precursor subset of flares. All data are normalized to the values at the start time of the flares. The plots display the averages for all events in the associated flare class. Flares outside of three standard deviations from the average and outside of 70° heliographic longitude are excluded. SHARP data are acquired from JSOC using the Python notebook created by Glogowski and Bobra (2016) and flare start times are identified by SWPC (2019).

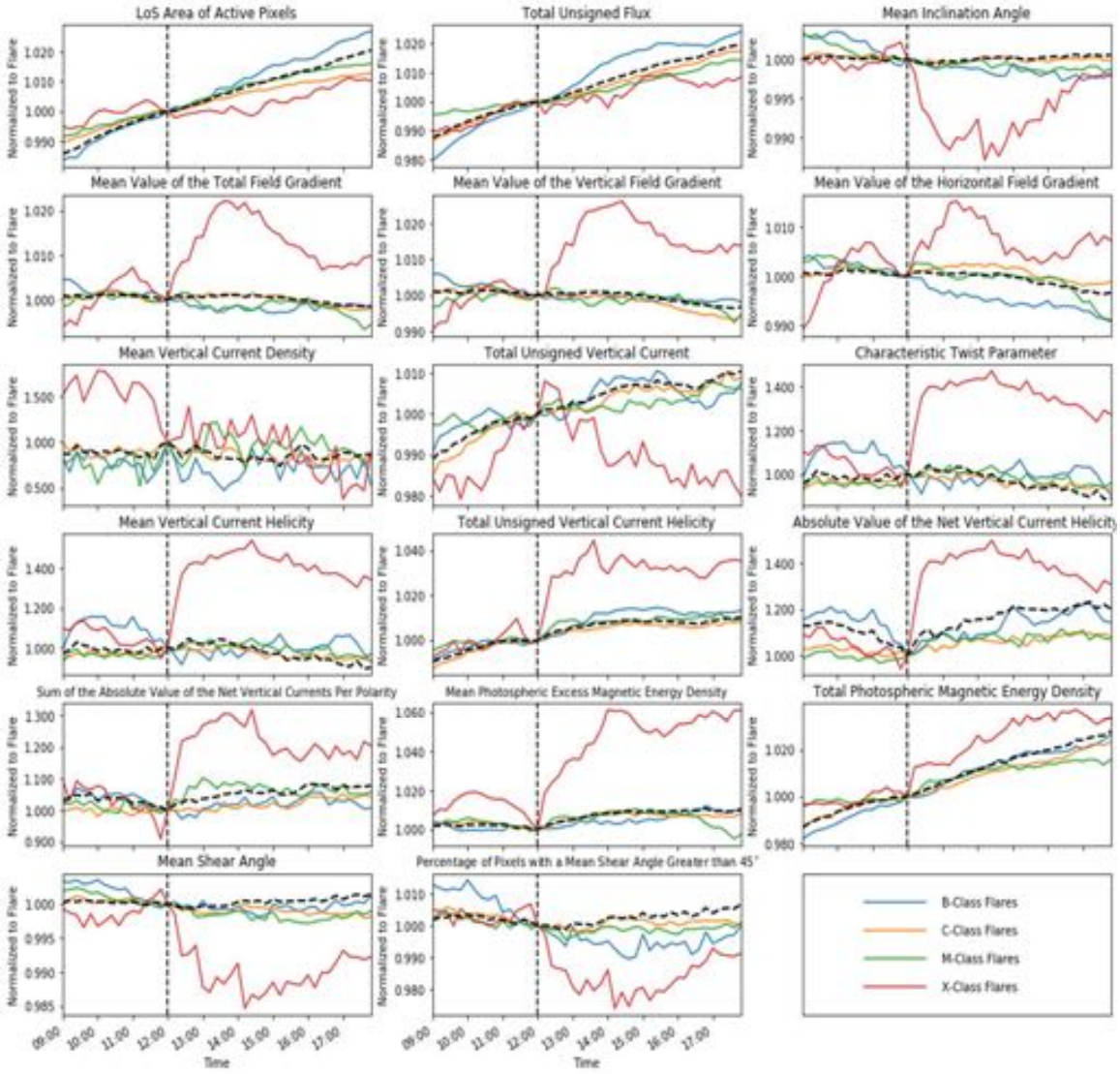

Figure 9. Epoch analysis for the 3-hour Precursor subset of flares. All data are normalized to the values at the start time of the flares. The plots display the averages for all events in the associated flare class. Flares outside of three standard deviations from the average and outside of 70° heliographic longitude are excluded. SHARP data are acquired from JSOC using the Python notebook created by Glogowski and Bobra (2016) and flare start times are identified by SWPC (2019).

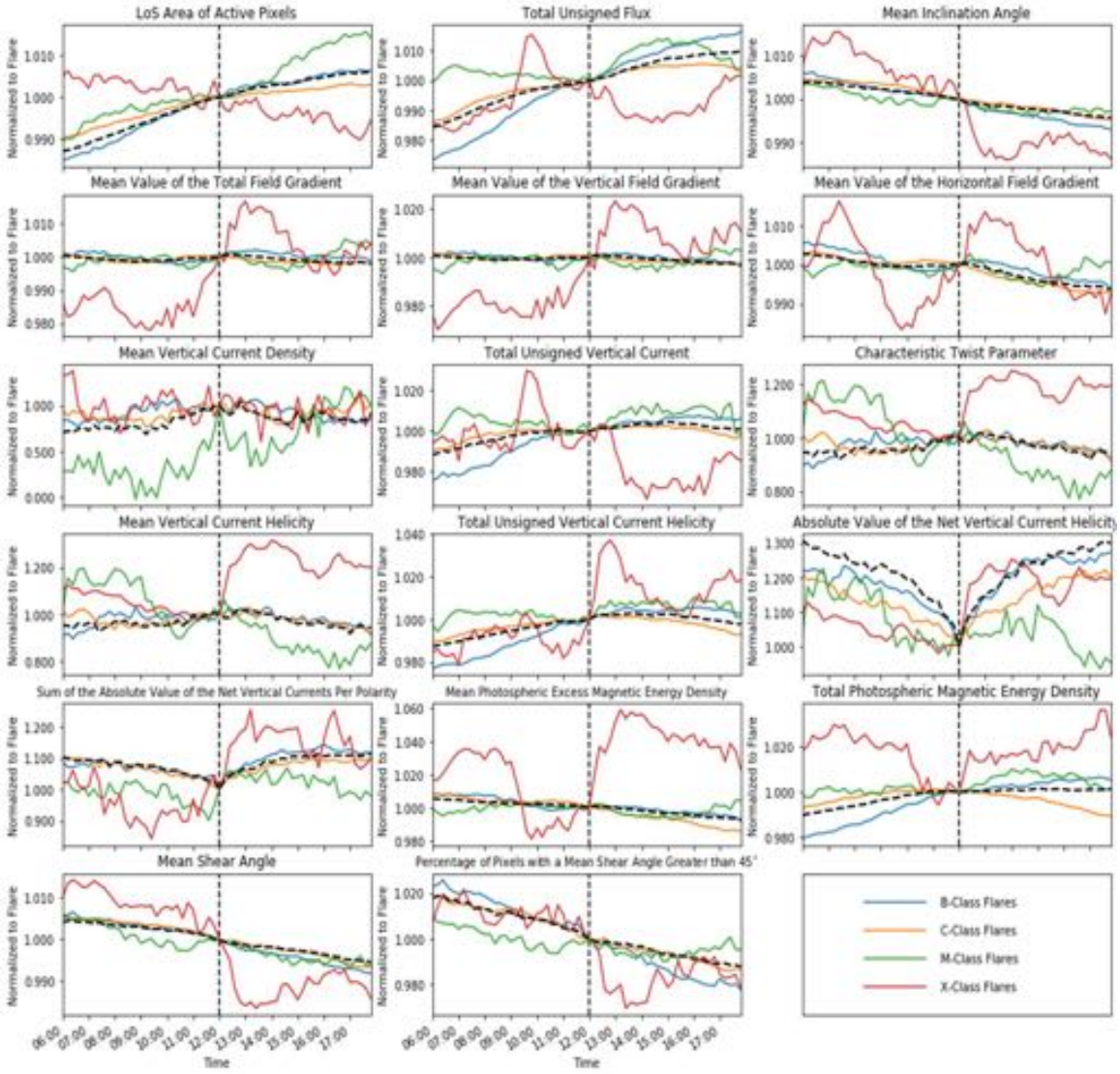

Figure 10. Epoch analysis for the 6-hour Non-Precursor subset of flares. All data are normalized to the values at the start time of the flares. The plots display the averages for all events in the associated flare class. Flares outside of three standard deviations from the average and outside of 70° heliographic longitude are excluded. SHARP data are acquired from JSOC using the Python notebook created by Glogowski and Bobra (2016) and flare start times are identified by SWPC (2019).

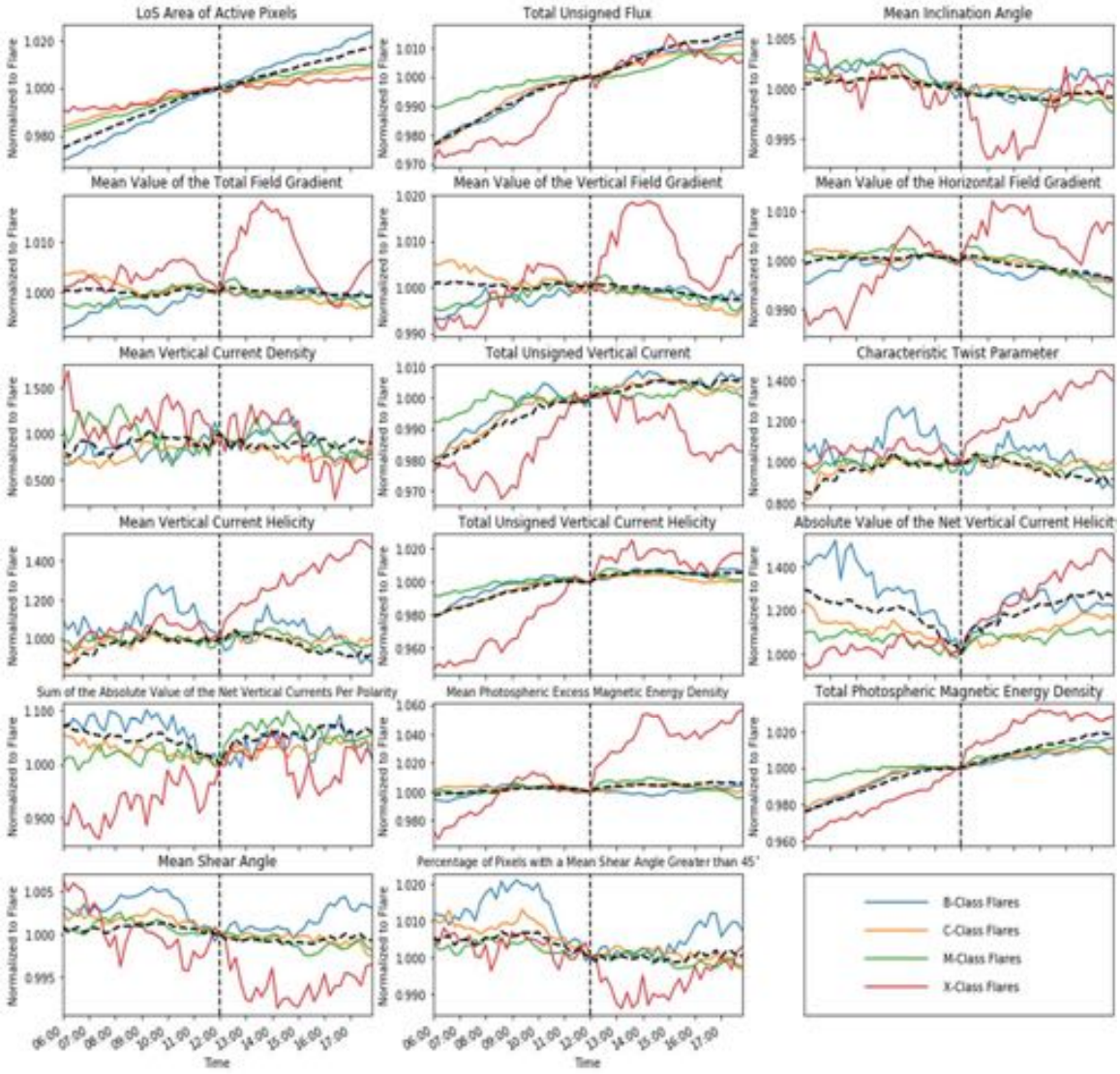

Figure 11. Epoch analysis for the 6-hour Precursor subset of flares. All data are normalized to the values at the start time of the flares. The plots display the averages for all events in the associated flare class. Flares outside of three standard deviations from the average and outside of 70° heliographic longitude are excluded. SHARP data are acquired from JSOC using the Python notebook created by Glogowski and Bobra (2016) and flare start times are identified by SWPC (2019).

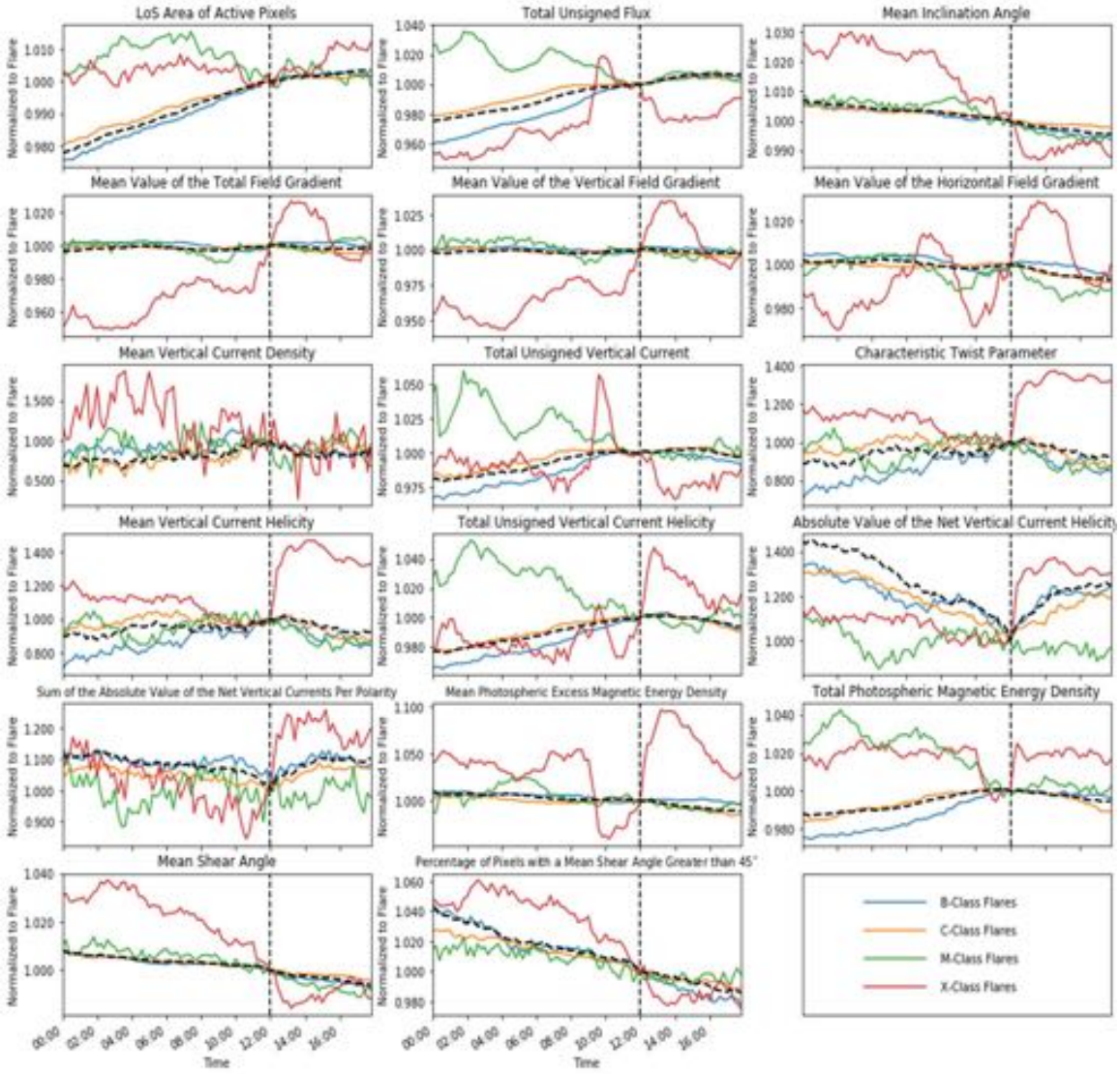

Figure 12. Epoch analysis for the 12-hour Non-Precursor subset of flares. All data are normalized to the values at the start time of the flares. The plots display the averages for all events in the associated flare class. Flares outside of three standard deviations from the average and outside of 70° heliographic longitude are excluded. SHARP data are acquired from JSOC using the Python notebook created by Glogowski and Bobra (2016) and flare start times are identified by SWPC (2019).

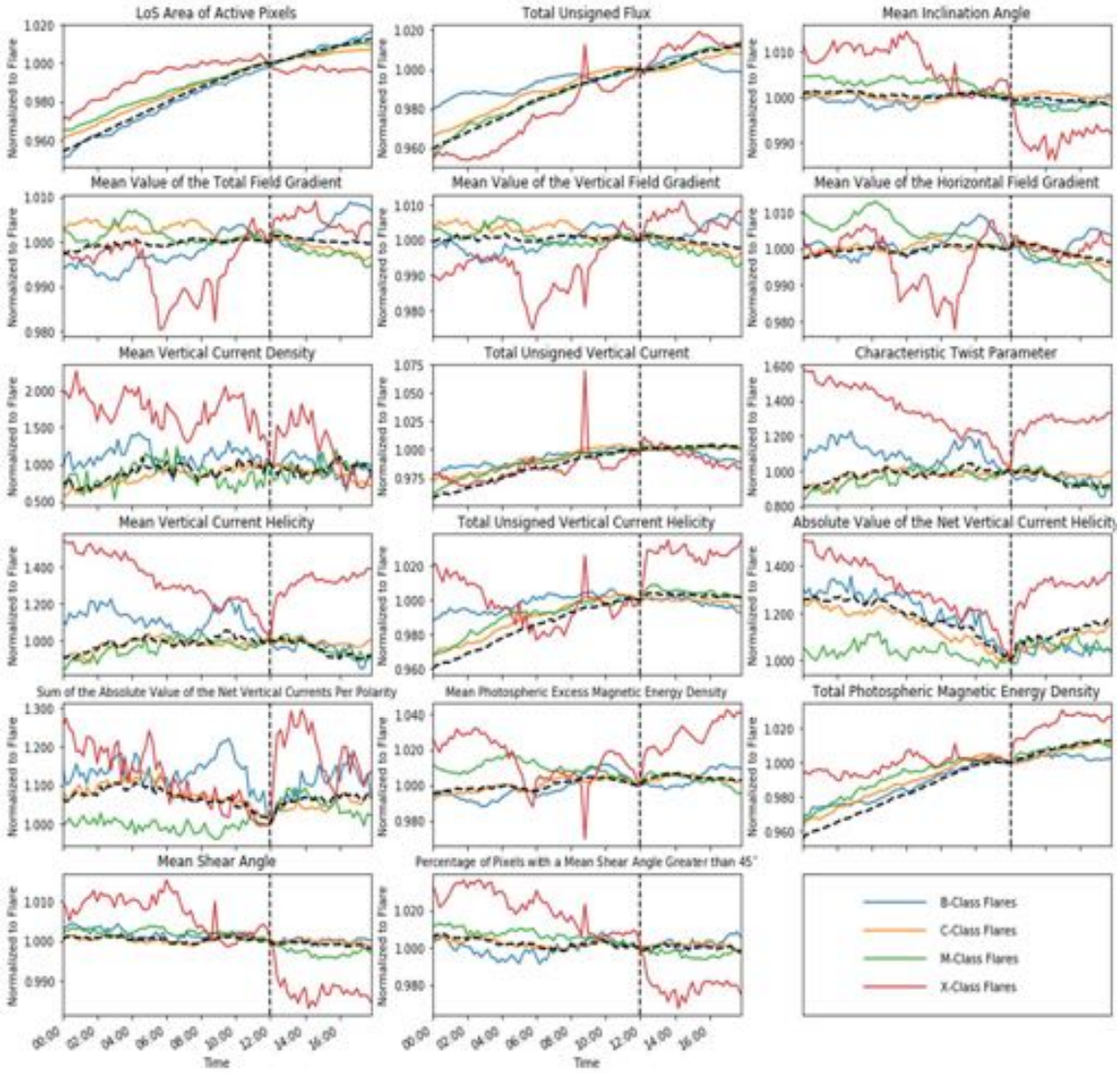

Figure 13. Epoch analysis for the 12-hour Precursor subset of flares. All data are normalized to the values at the start time of the flares. The plots display the averages for all events in the associated flare class. Flares outside of three standard deviations from the average and outside of 70° heliographic longitude are excluded. SHARP data are acquired from JSOC using the Python notebook created by Glogowski and Bobra (2016) and flare start times are identified by SWPC (2019).

V. Conclusions

5.1 Summary

The two primary points of investigation in this analysis were to identify and compare the trends of (1) differing flare classes for varying time intervals leading up to an event, and (2) of flares that occur with and without a precursor flare, with the ultimate goal of detecting potential signatures within the photospheric magnetic field of magnetic reconnection associated with solar flare occurrence. In reference to (1), the data showed no significant time dependence of the SHARP parameters for the differing flare strengths. Though there may be a relationship between the different flare classes and the amount of time it takes for enough energy to build up over the AR – on the order of 24 hours for X-class flares and a couple hours for B- and C-class flares – the SHARP parameters do not show this same relationship.

Regarding (2), there are clear differences in the magnetic conditions of an AR during solar flare events that occur with a precursor(s) versus those that occur without. In particular, SHARP parameters associated with an AR's size, energy, and shear showed the most discernable differences in trends/behavior. For AR size and energy, all flare classes showed more continuous increase prior to and following flare occurrence for flares that had a precursor(s), while those without showed leveling off or a decreasing trend. This suggests that ARs that produce flares with precursors are continuing to evolve and appreciably more complex than those that produce a flare without a precursor. Of note, X-class flares showed the most drastic difference in trends for flares with and without a precursor(s), with the implication that ARs that have an X-class flare occur with no

precursor may have reached maximum growth, while those that produce X-class flares with a precursor(s) could still be growing and evolving. For shear related parameters, the data indicated that for all flare classes shear across the AR is enhanced by the occurrence of a precursor, agreeing with the findings of Verma (2018).

In a way, the analysis of the SHARP parameters for flares that occur with and without a precursor(s) is validation of the rule of thumb of flare persistence (Sawyer et al., 1986). The data shows that a flare that occurs with a precursor is likely associated with a more complex and evolving AR, and that the precursor even helps set up the conditions for further flaring. Thus, an AR that has flared recently (the precursor) is likely to flare again (the main flare). Note that this interpretation does not take into account smaller flares that occur after a larger flare – i.e. an "aftershock" flare – which would also play into flare persistence.

Though the data in this analysis provided insights on the conditions of the magnetic structures of an AR for varying flare classes and situations (precursor/no precursor) during solar flare events, ultimately none of the SHARP parameters showed a distinct signature of magnetic reconnection. As stated previously, magnetic reconnection during a solar flare event occurs higher in the solar atmosphere in the corona and chromosphere. With that, it is likely that any distinct signature of reconnection within the various magnetic parameters exists within coronal and chromospheric magnetic field data – which as of now cannot be directly measured – and the signature is subdued/lost at lower altitudes within the photospheric magnetic field.

5.2 Future Work

The present study expanded upon the work of Whitney (2020) by separating the solar flares used in the analysis by not only maximum x-ray flux – i.e. flare class – but by the occurrence of a precursor flare. The additional separation/classification of flares based on commonalities of the flare event or AR helps to highlight the trends in magnetic parameters during these events that may be washed out when flares of different situations and with different magnetic conditions of the AR are averaged together. Furthermore, the additional classification within the analysis provides insights on the specific trends and behavior during events with a particular setup that can benefit forecasters who observe similar scenarios and conditions. Further break down of the solar flare database and analysis of the trends of different flaring scenarios will provide more insights for flare events of all different conditions. Other traits of the flare events or ARs that could be used for additional classification of the solar flare database include (Whitney, 2020):

- Flares that occur near solar meridian versus those that occur near solar limbs – requiring a correction of limb darkening effects such as that in Criscuoli et al. (2017)
- Flares that occur with an associated CME versus those without such an event
- Flares whose duration is on the order of a few minutes versus those that last an hour or more.

The analysis performed in this study looked at data that was at most 24 hours before and 6 hours after a solar flare event. Examining the data throughout the entire evolution of the ARs would provide further insight into the magnetic field of an AR when it is and is

not flaring, which would improve the understanding of why an AR produces a solar flare. Furthermore, the SHARP is a patch that is large enough to capture the entire AR; further work toward narrowing the patch to minimize the amount of quiet photosphere counted should improve results. Along those lines, similar to Bobra and Couvidat (2015) and Mason and Hoeksema (2010), calculating the parameters based on pixels that are only along the PIL would isolate the data to the region of flaring within an AR, ignoring areas of weaker magnetic fields. Finally, it is uncertain exactly how the energy deposition from solar flares (particularly strong flares) into the solar atmosphere changes the atmospheric chemistry and opacity. Such changes may cause the Stokes parameters – used to calculate the vector magnetic components – to be perturbed. Future work investigating such perturbations would help to better understand the behavior of observed data following flare occurrence, as well as identify potential necessary corrections to the Stokes parameters in order to accurately calculate the vector magnetic components.

Appendix A

Standard Deviation Ranges

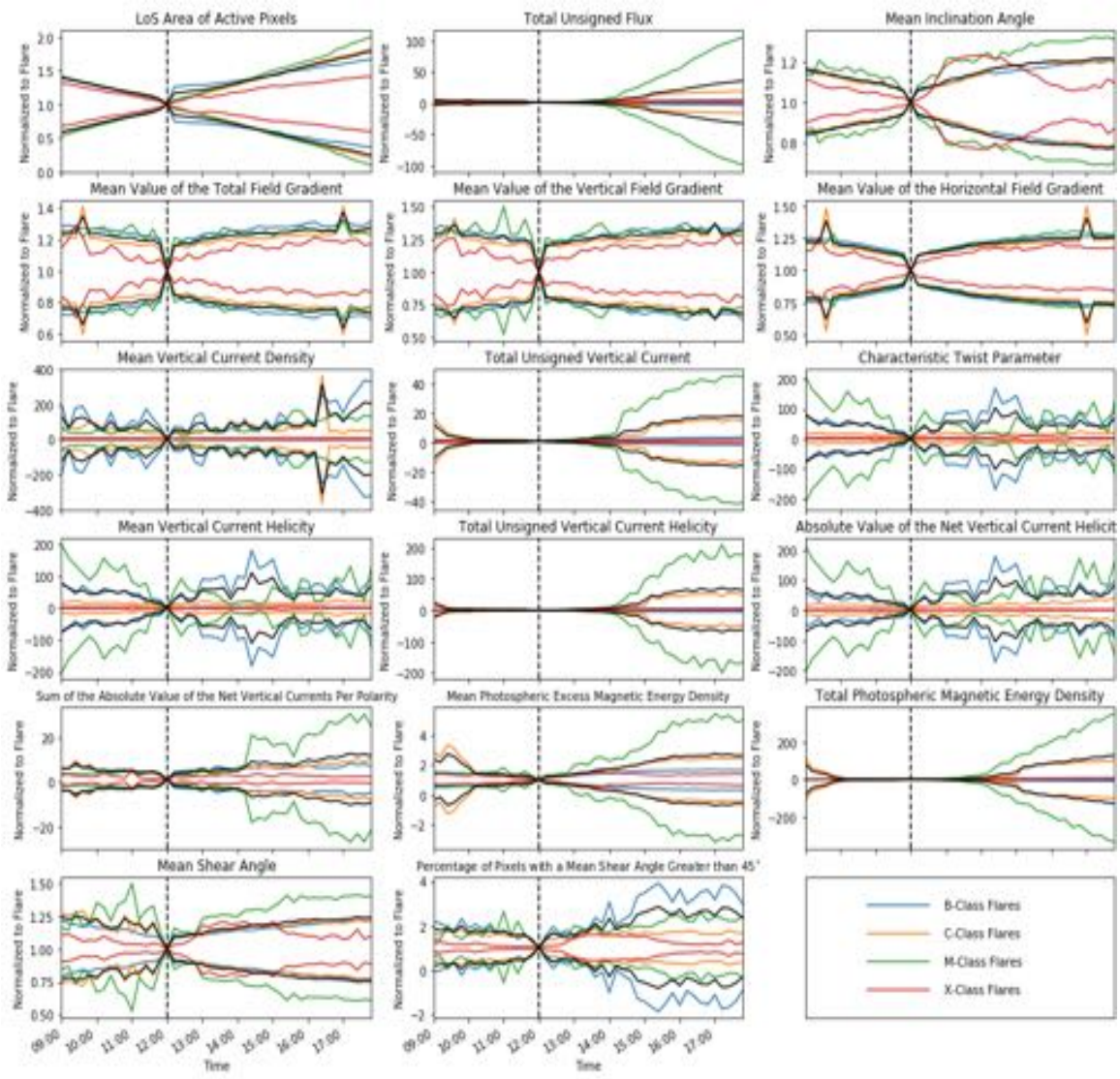

Figure 14. Standard deviation limits applied to the 3-hour General subset. Data outside these limits are disregarded for this study. Plotted lines represent three standard deviations from the average values. Colored lines represent different flare classes as denoted; the black line represents data for all flares. Values are normalized to flare start times, denoted by the vertical dashed line. SHARP data are acquired from JSOC using the Python notebook created by Glogowski and Bobra (2016) and are times are identified by SWPC (2019).

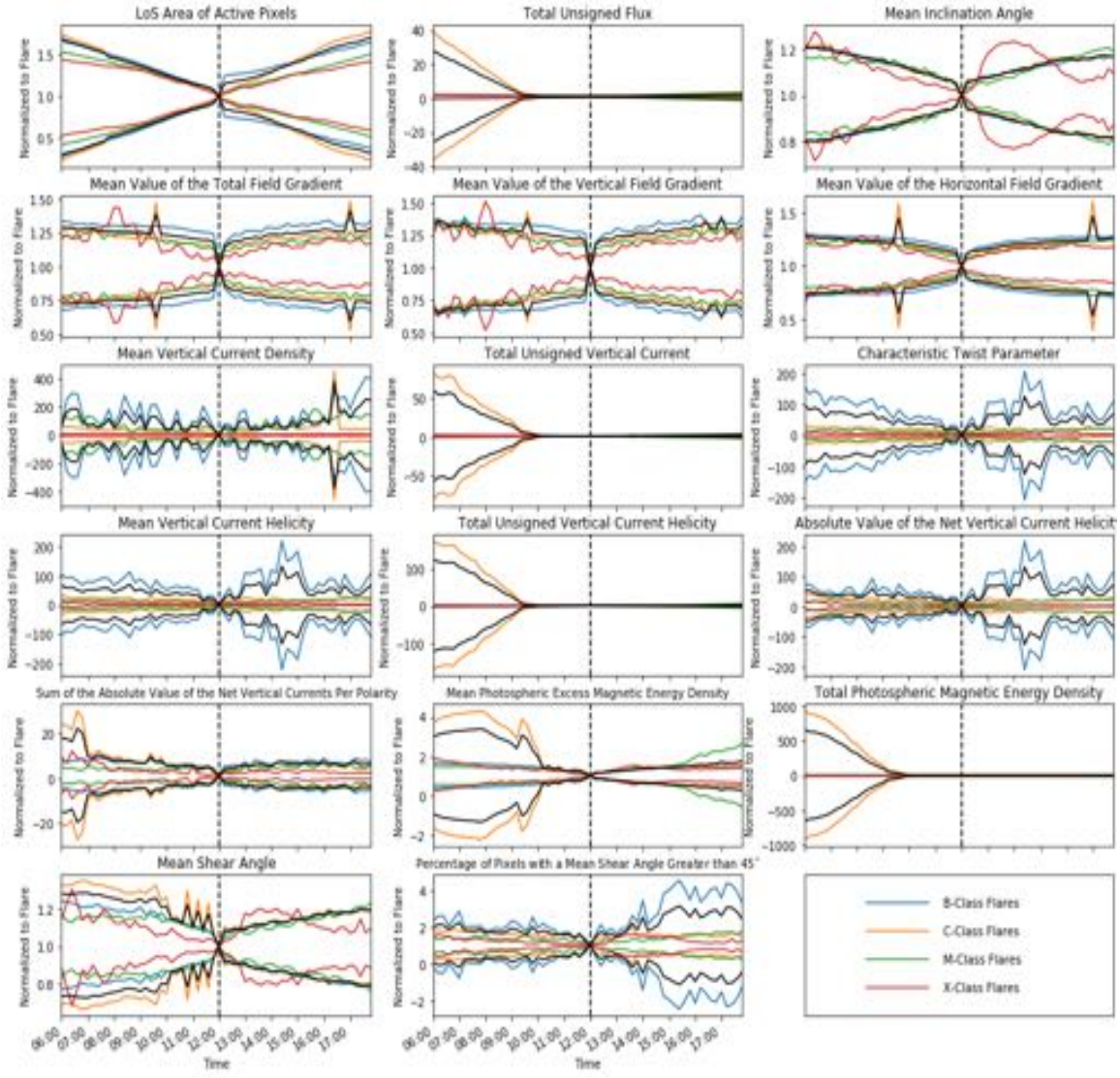

Figure 15. Standard deviation limits applied to the 6-hour General subset. Data outside these limits are disregarded for this study. Plotted lines represent three standard deviations from the average values. Colored lines represent different flare classes as denoted; the black line represents data for all flares. Values are normalized to flare start times, denoted by the vertical dashed line. SHARP data are acquired from JSOC using the Python notebook created by Glogowski and Bobra (2016) and are times are identified by SWPC (2019).

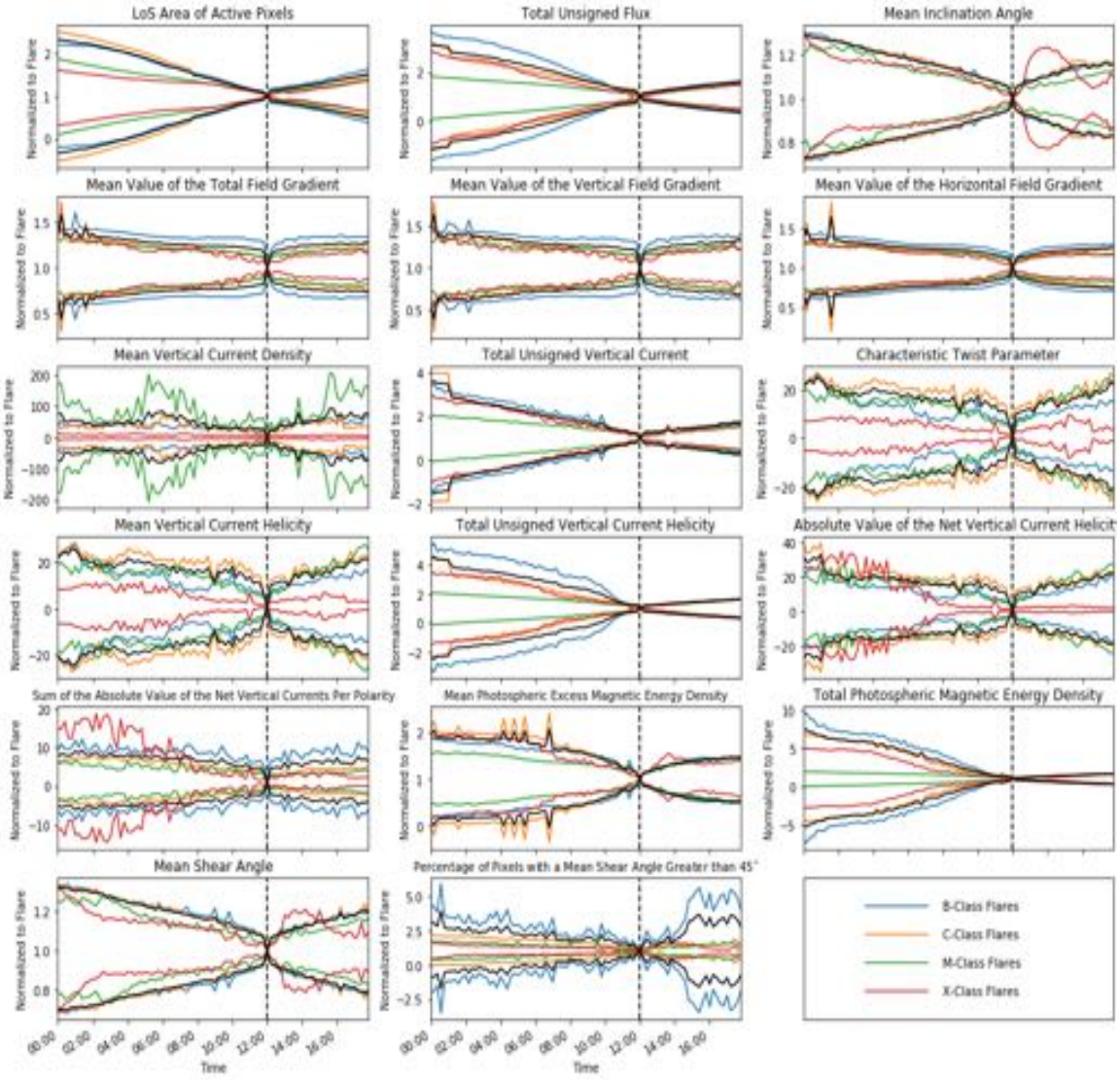

Figure 16. Standard deviation limits applied to the 12-hour General subset. Data outside these limits are disregarded for this study. Plotted lines represent three standard deviations from the average values. Colored lines represent different flare classes as denoted; the black line represents data for all flares. Values are normalized to flare start times, denoted by the vertical dashed line. SHARP data are acquired from JSOC using the Python notebook created by Glogowski and Bobra (2016) and are times are identified by SWPC (2019).

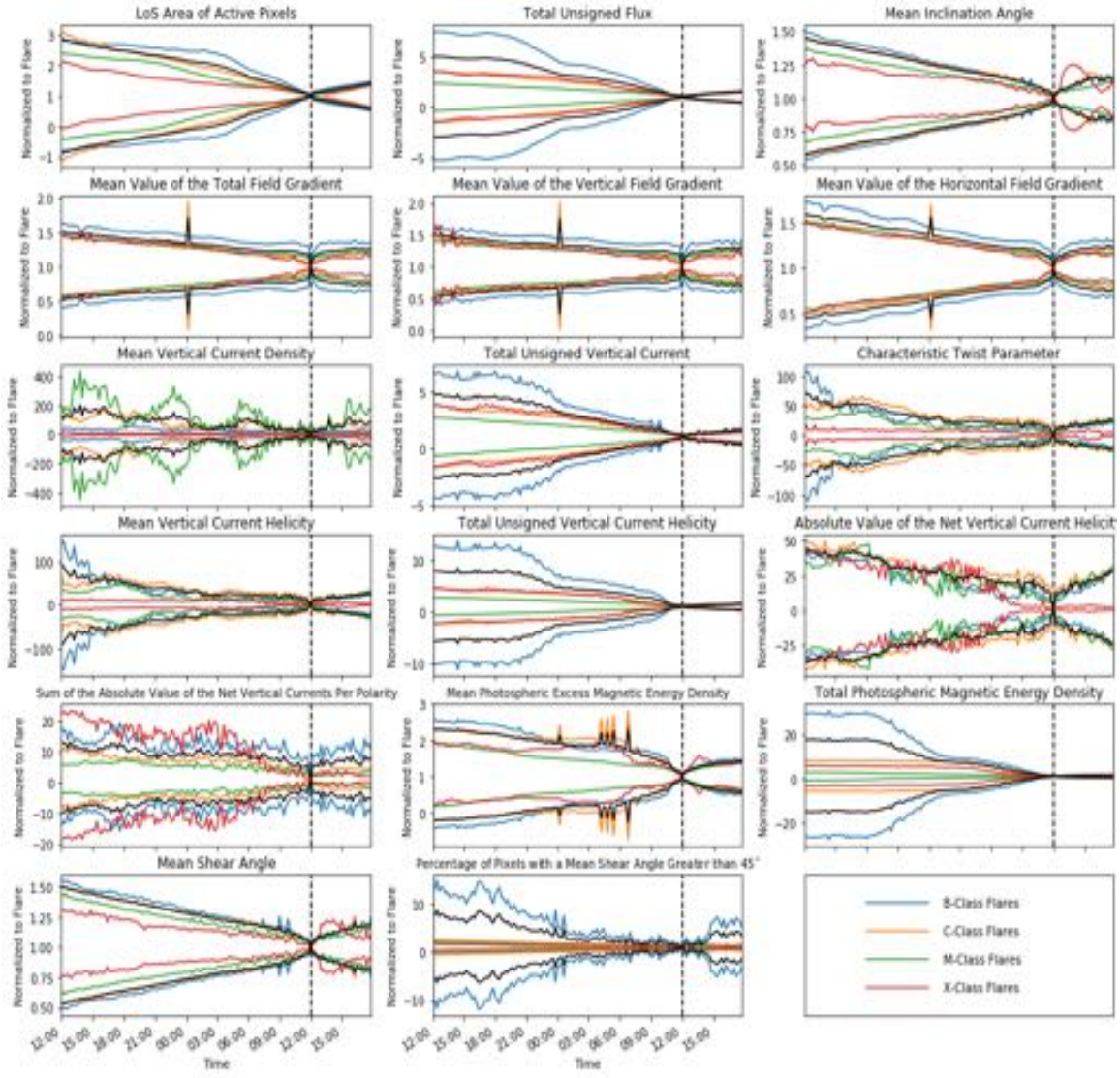

Figure 17. Standard deviation limits applied to the 24-hour General subset. Data outside these limits are disregarded for this study. Plotted lines represent three standard deviations from the average values. Colored lines represent different flare classes as denoted; the black line represents data for all flares. Values are normalized to flare start times, denoted by the vertical dashed line. SHARP data are acquired from JSOC using the Python notebook created by Glogowski and Bobra (2016) and are times are identified by SWPC (2019).

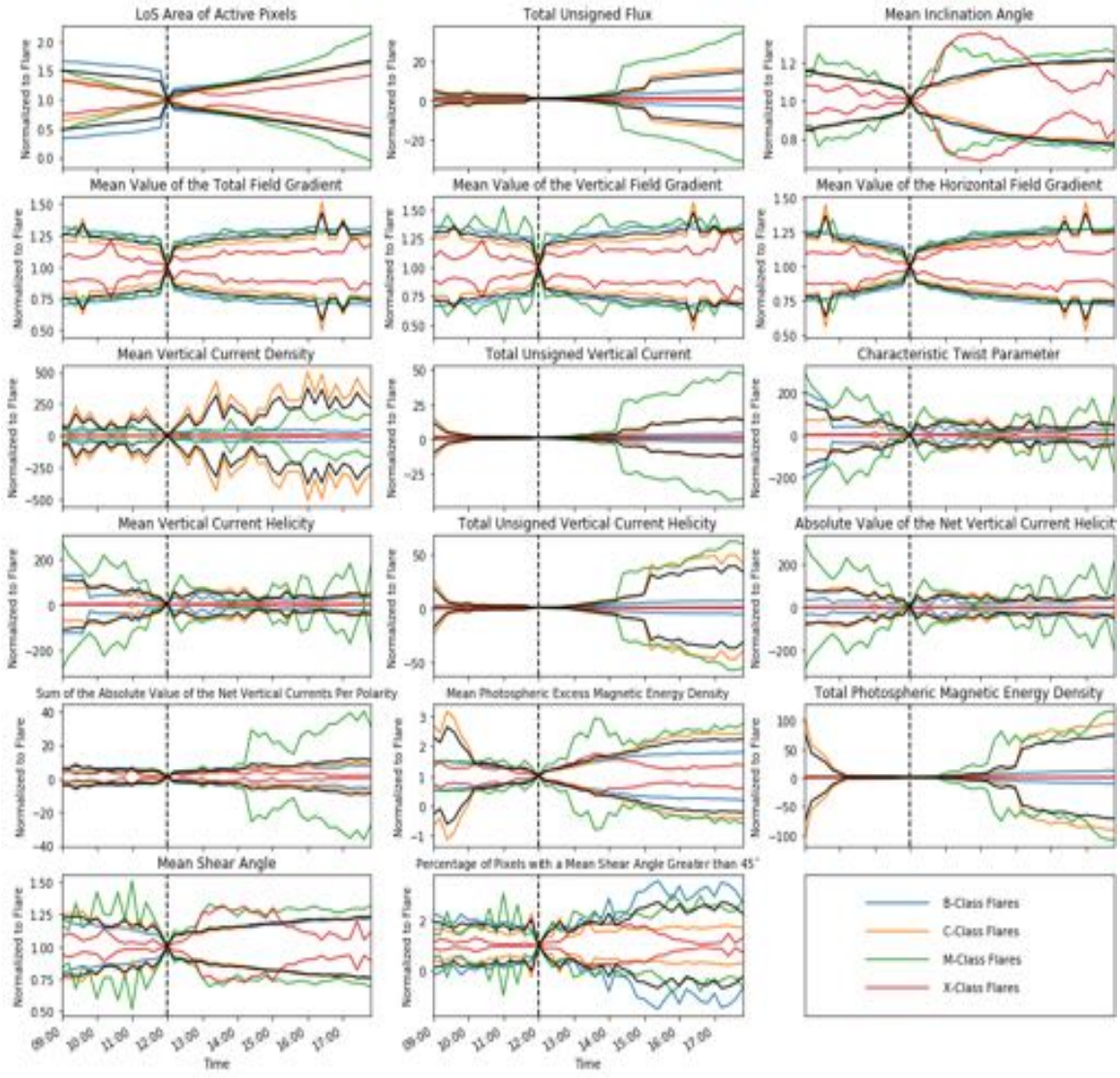

Figure 18. Standard deviation limits applied to the 3-hour Non-Precursor subset. Data outside these limits are disregarded for this study. Plotted lines represent three standard deviations from the average values. Colored lines represent different flare classes as denoted; the black line represents data for all flares. Values are normalized to flare start times, denoted by the vertical dashed line. SHARP data are acquired from JSOC using the Python notebook created by Glogowski and Bobra (2016) and are times are identified by SWPC (2019).

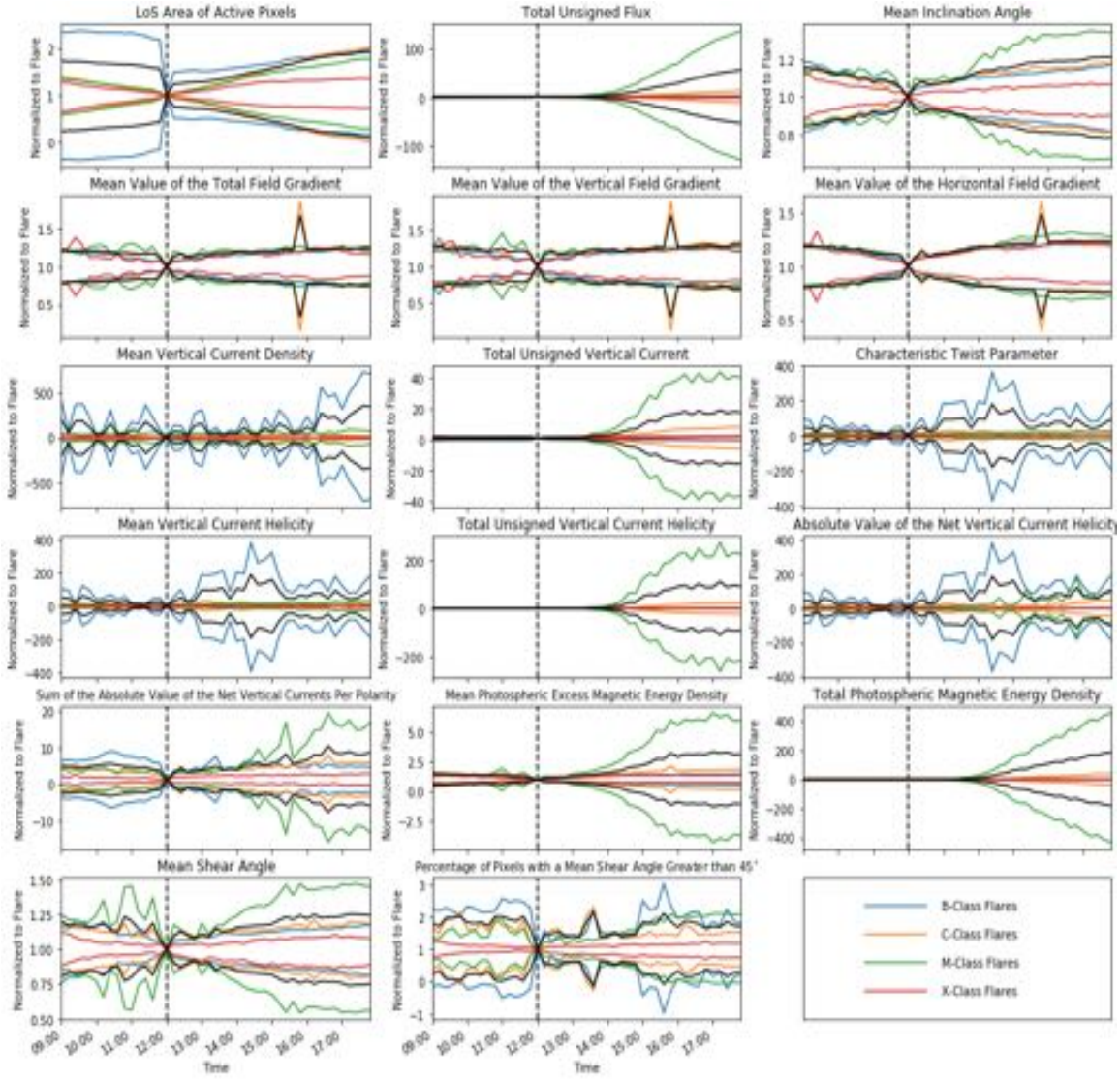

Figure 19. Standard deviation limits applied to the 3-hour Precursor subset. Data outside these limits are disregarded for this study. Plotted lines represent three standard deviations from the average values. Colored lines represent different flare classes as denoted; the black line represents data for all flares. Values are normalized to flare start times, denoted by the vertical dashed line. SHARP data are acquired from JSOC using the Python notebook created by Glogowski and Bobra (2016) and are times are identified by SWPC (2019).

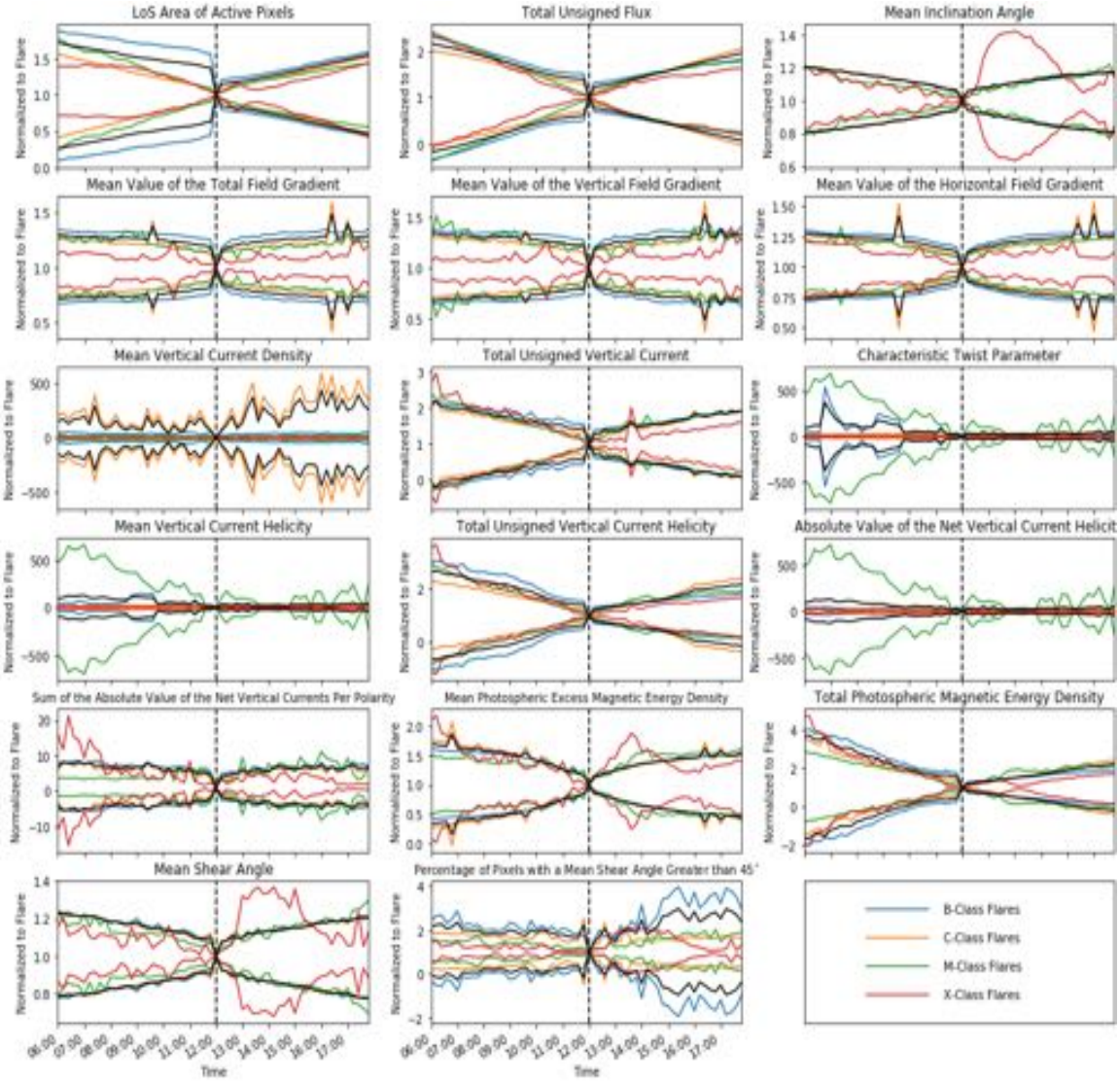

Figure 20. Standard deviation limits applied to the 6-hour Non-Precursor subset. Data outside these limits are disregarded for this study. Plotted lines represent three standard deviations from the average values. Colored lines represent different flare classes as denoted; the black line represents data for all flares. Values are normalized to flare start times, denoted by the vertical dashed line. SHARP data are acquired from JSOC using the Python notebook created by Glogowski and Bobra (2016) and are times are identified by SWPC (2019).

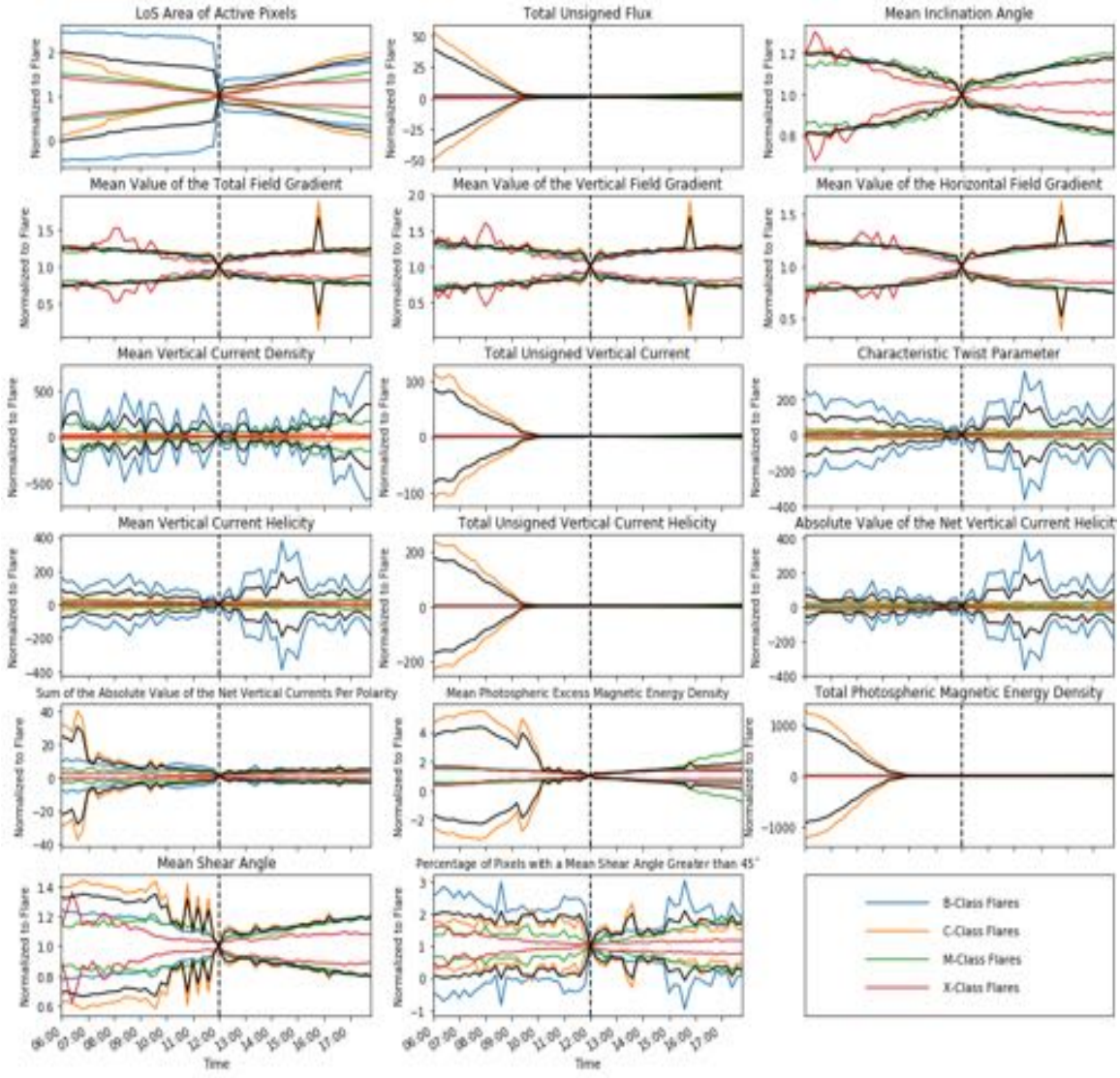

Figure 21. Standard deviation limits applied to the 6-hour Precursor subset. Data outside these limits are disregarded for this study. Plotted lines represent three standard deviations from the average values. Colored lines represent different flare classes as denoted; the black line represents data for all flares. Values are normalized to flare start times, denoted by the vertical dashed line. SHARP data are acquired from JSOC using the Python notebook created by Glogowski and Bobra (2016) and are times are identified by SWPC (2019).

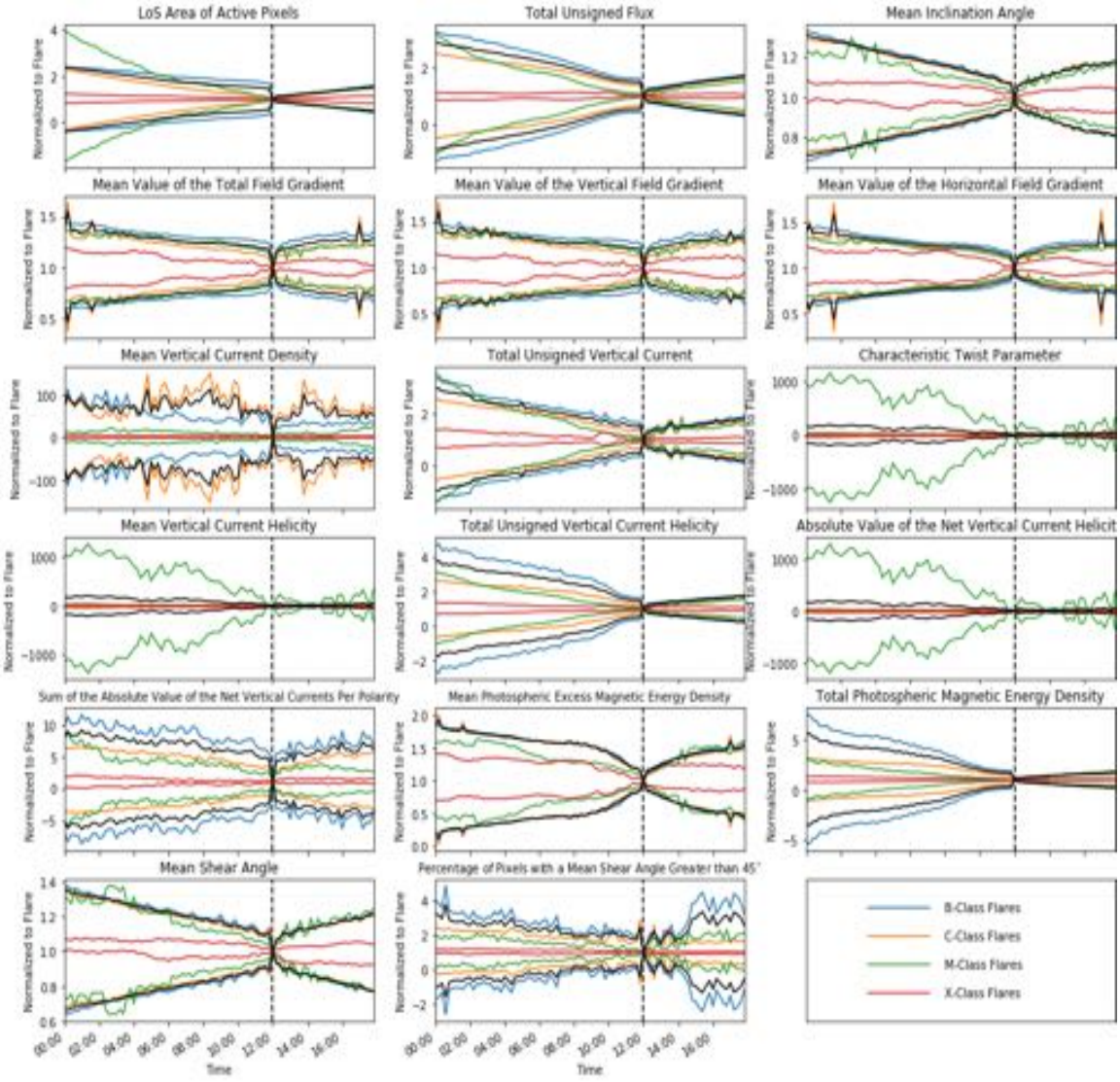

Figure 22. Standard deviation limits applied to the 12-hour Non-Precursor subset. Data outside these limits are disregarded for this study. Plotted lines represent three standard deviations from the average values. Colored lines represent different flare classes as denoted; the black line represents data for all flares. Values are normalized to flare start times, denoted by the vertical dashed line. SHARP data are acquired from JSOC using the Python notebook created by Glogowski and Bobra (2016) and are times are identified by SWPC (2019).

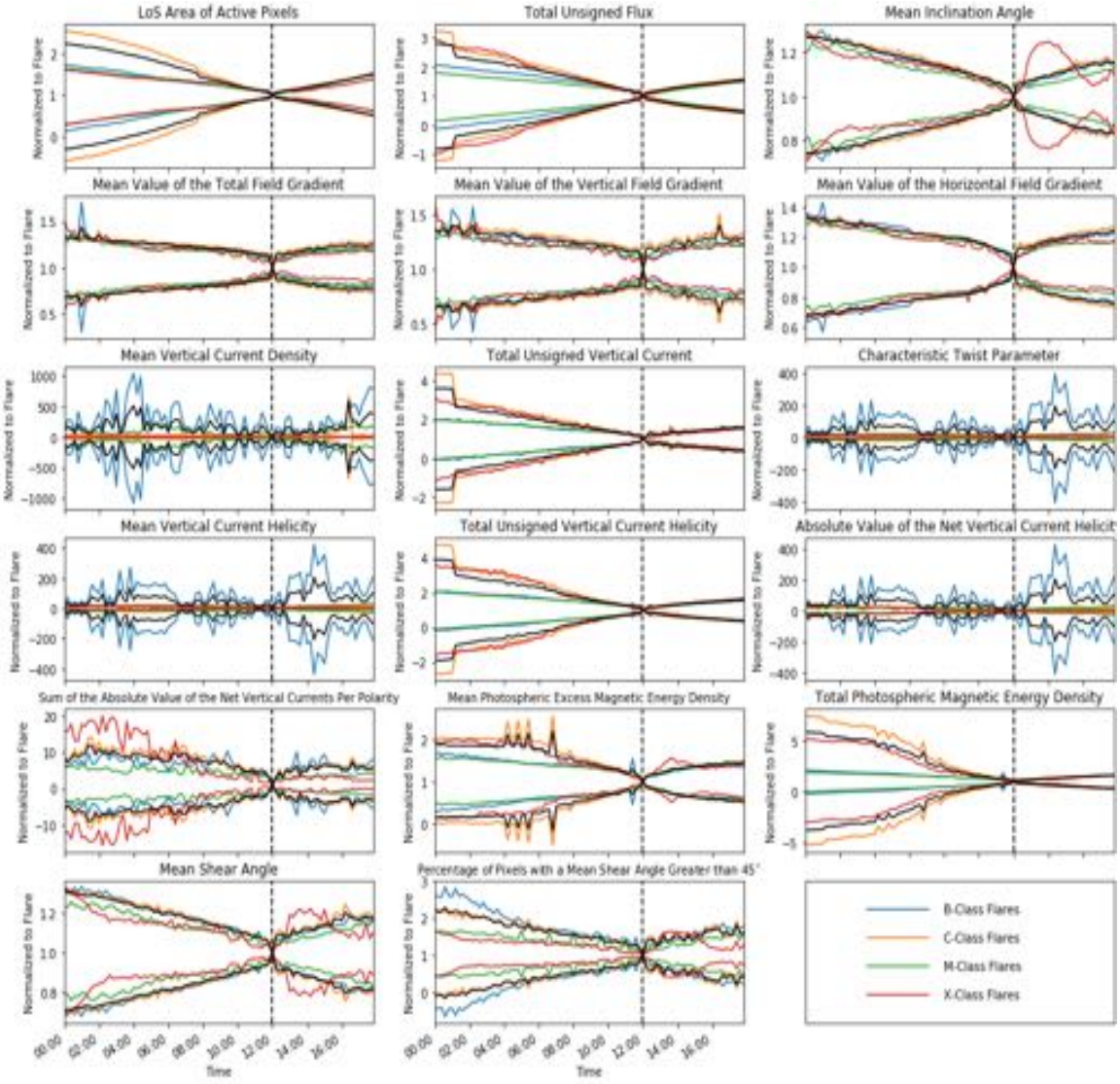

Figure 23. Standard deviation limits applied to the 12-hour Precursor subset. Data outside these limits are disregarded for this study. Plotted lines represent three standard deviations from the average values. Colored lines represent different flare classes as denoted; the black line represents data for all flares. Values are normalized to flare start times, denoted by the vertical dashed line. SHARP data are acquired from JSOC using the Python notebook created by Glogowski and Bobra (2016) and are times are identified by SWPC (2019).

Appendix B

Plots without X-class Data

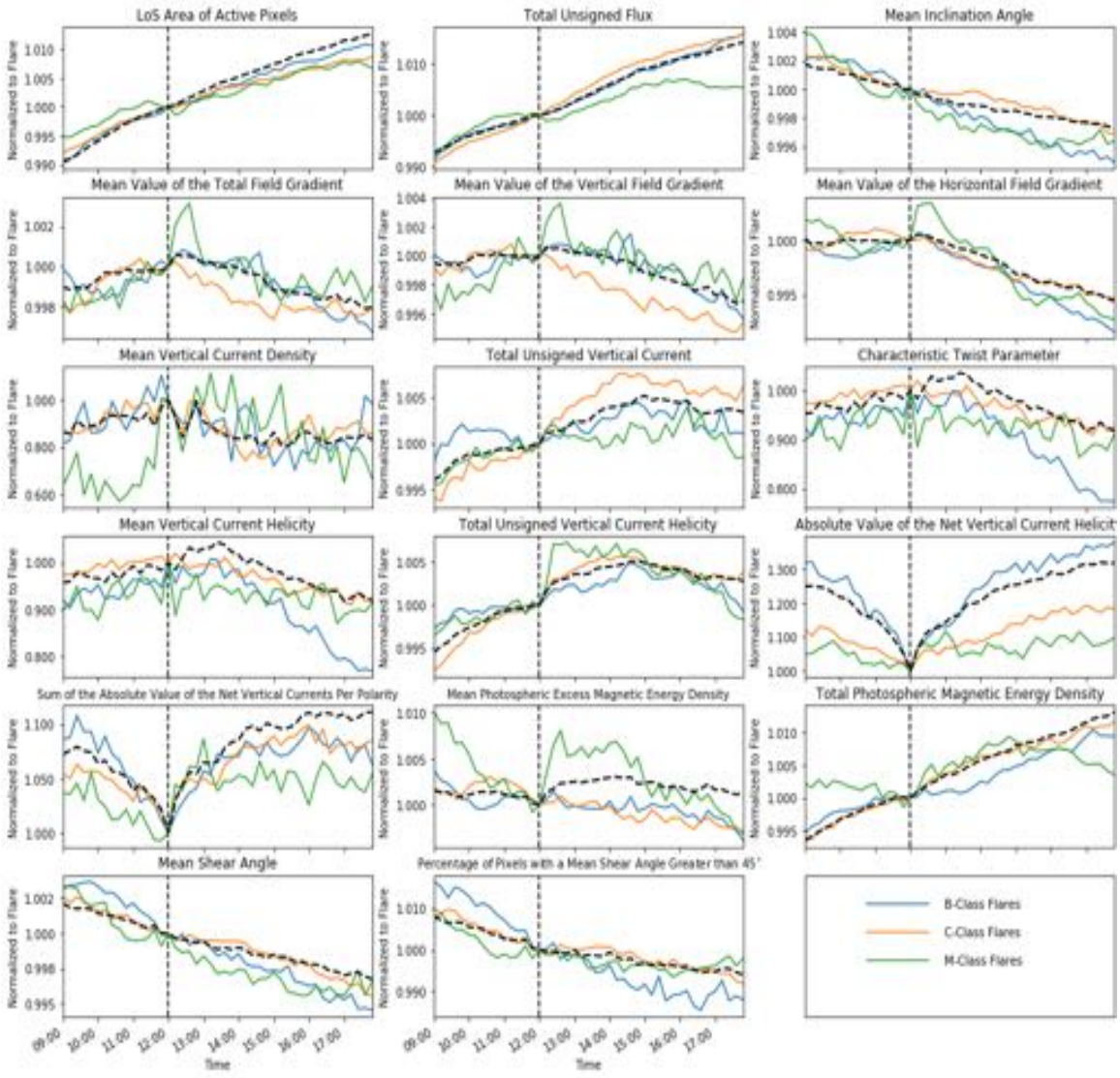

Figure 24. Epoch analysis for the 3-hour General subset of flares without X-class data plotted. All data are normalized to the values at the start time of the flares. The plots display the averages for all events in the associated flare class. Flares outside of three standard deviations from the average and outside of 70° heliographic longitude are excluded. SHARP data are acquired from JSOC using the Python notebook created by Glogowski and Bobra (2016) and flare start times are identified by SWPC (2019).

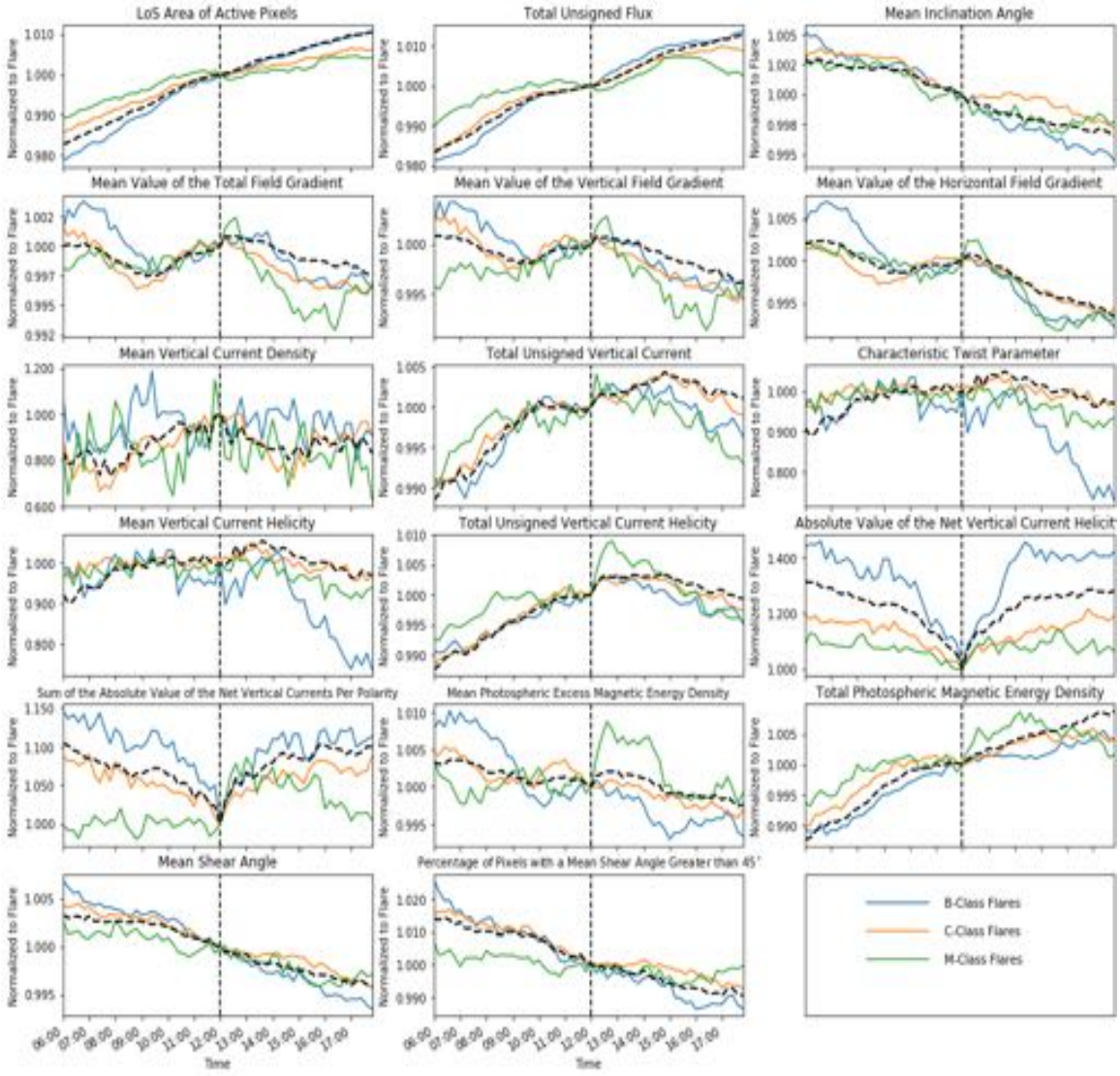

Figure 25. Epoch analysis for the 6-hour General subset of flares without X-class data plotted. All data are normalized to the values at the start time of the flares. The plots display the averages for all events in the associated flare class. Flares outside of three standard deviations from the average and outside of 70° heliographic longitude are excluded. SHARP data are acquired from JSOC using the Python notebook created by Glogowski and Bobra (2016) and flare start times are identified by SWPC (2019).

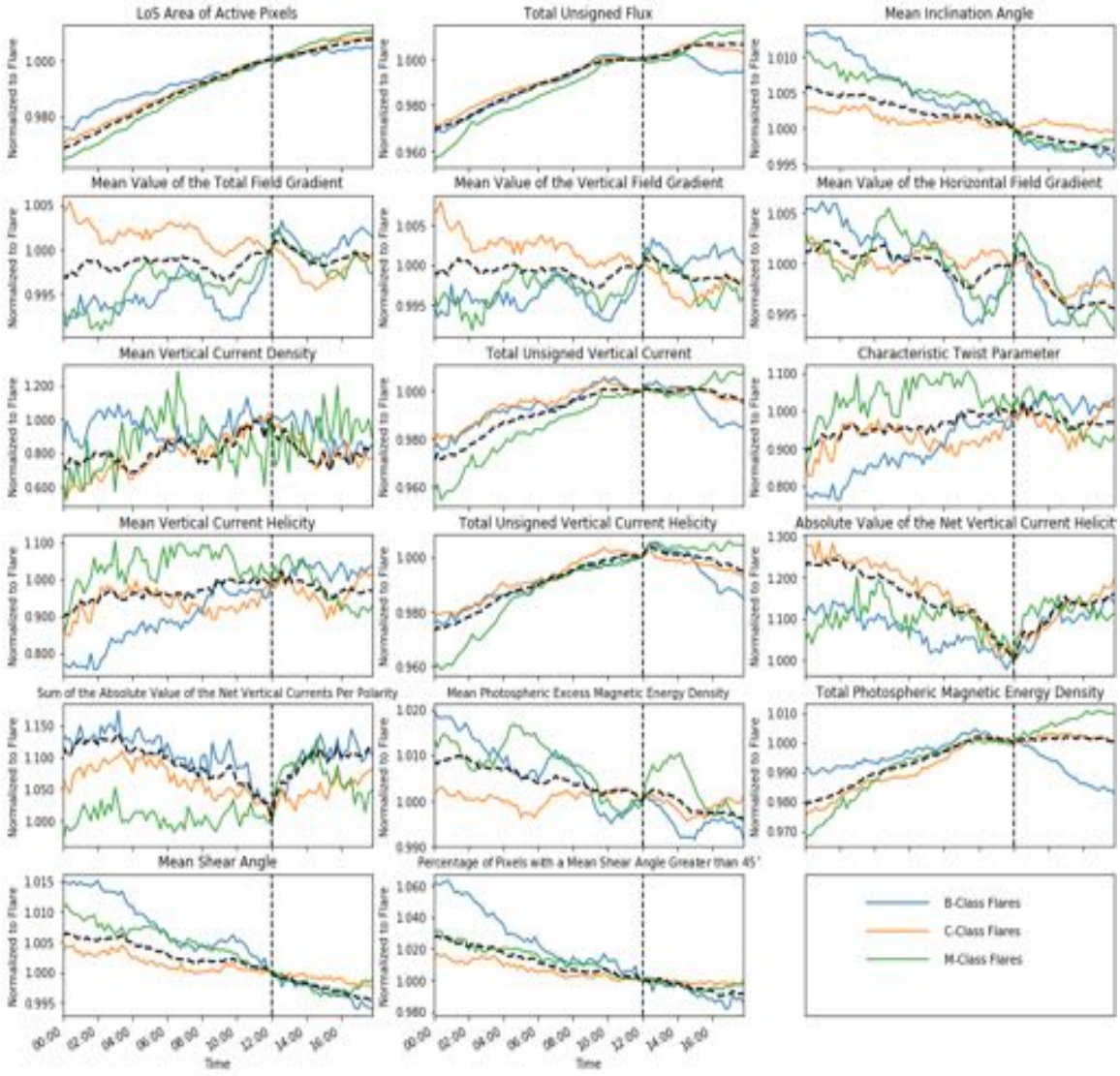

Figure 26. Epoch analysis for the 12-hour General subset of flares without X-class data plotted. All data are normalized to the values at the start time of the flares. The plots display the averages for all events in the associated flare class. Flares outside of three standard deviations from the average and outside of 70° heliographic longitude are excluded. SHARP data are acquired from JSOC using the Python notebook created by Glogowski and Bobra (2016) and flare start times are identified by SWPC (2019).

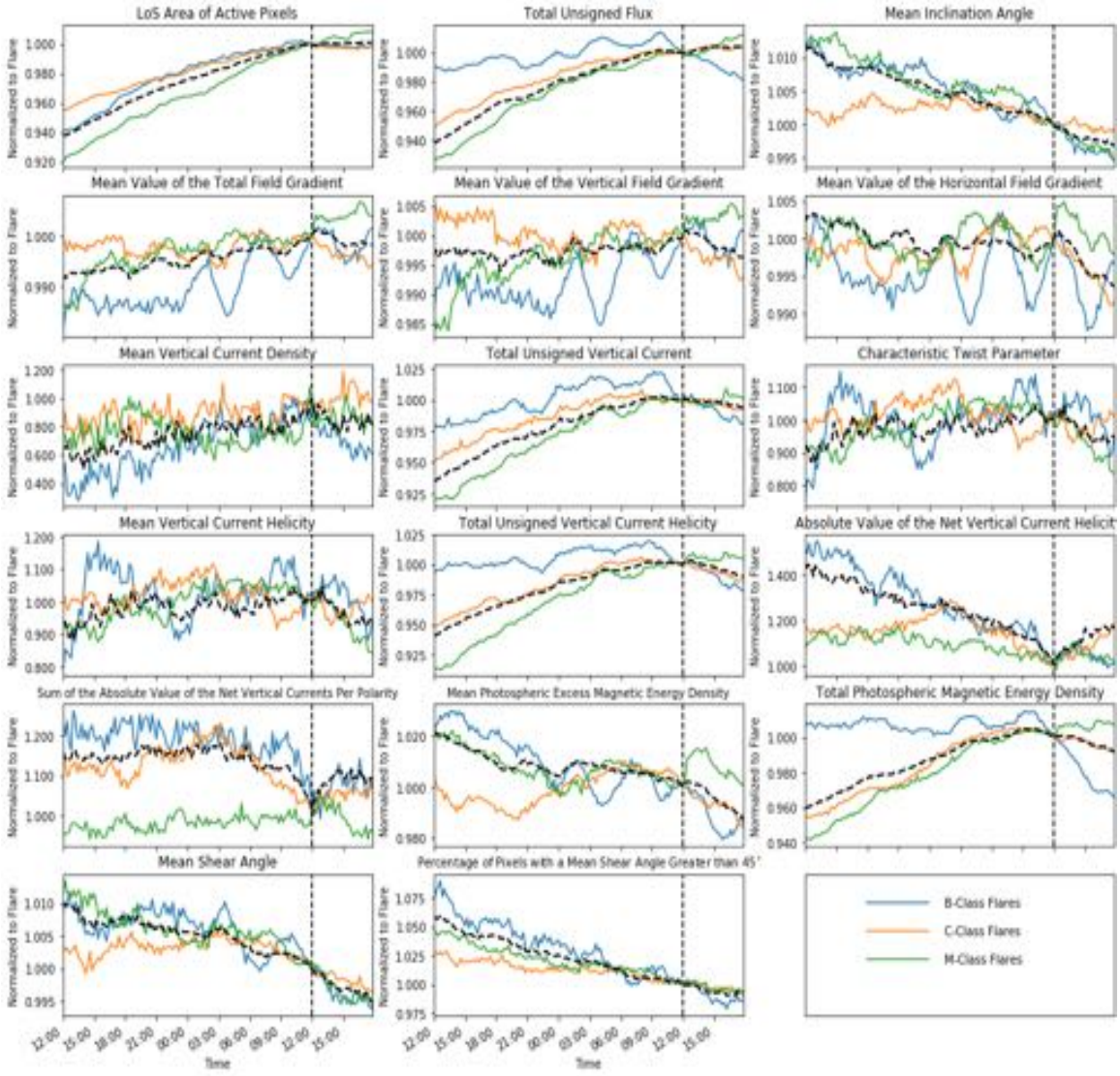

Figure 27. Epoch analysis for the 24-hour General subset of flares without X-class data plotted. All data are normalized to the values at the start time of the flares. The plots display the averages for all events in the associated flare class. Flares outside of three standard deviations from the average and outside of 70° heliographic longitude are excluded. SHARP data are acquired from JSOC using the Python notebook created by Glogowski and Bobra (2016) and flare start times are identified by SWPC (2019).

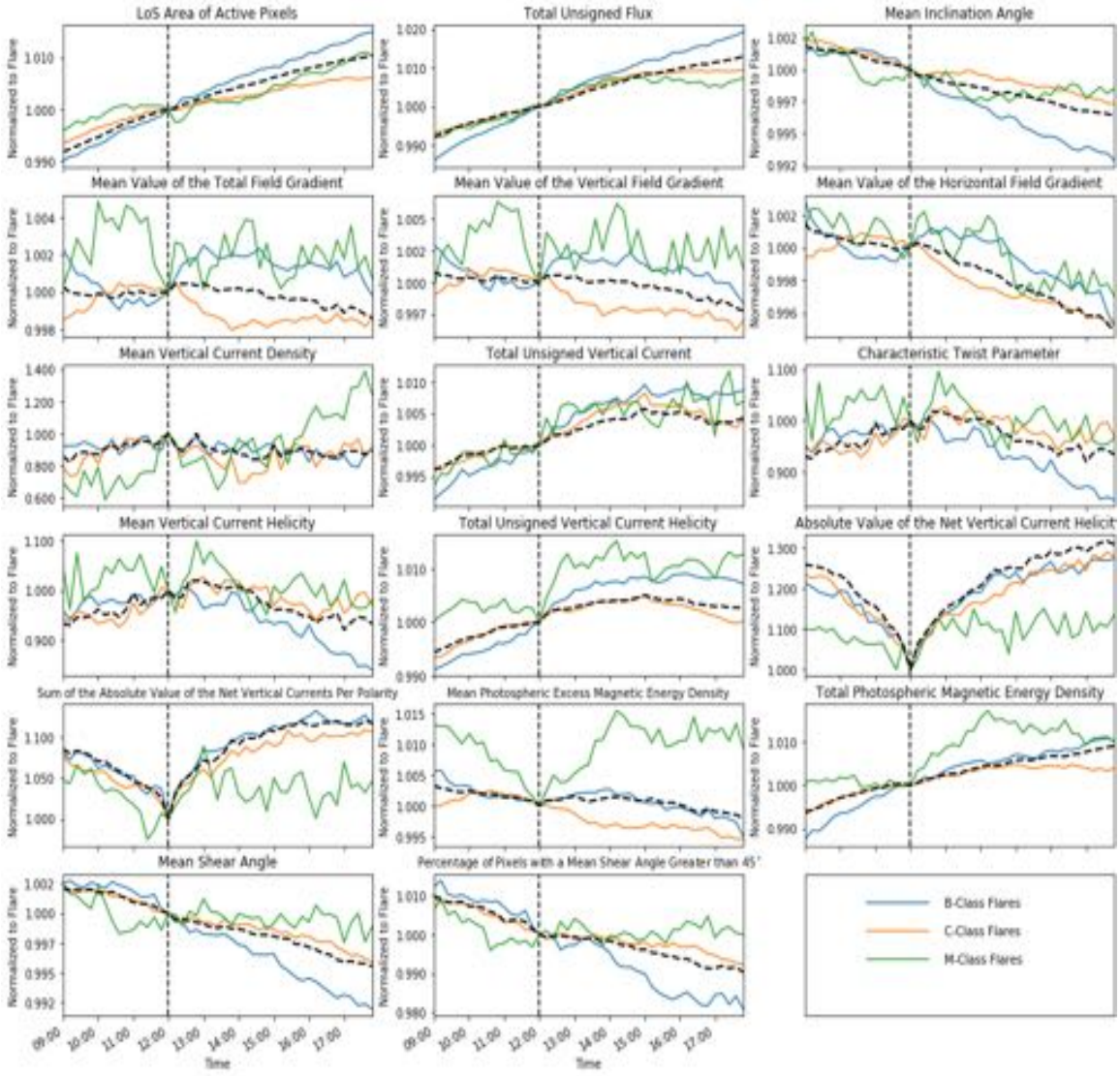

Figure 28. Epoch analysis for the 3-hour Non-Precursor subset of flares without X-class data plotted. All data are normalized to the values at the start time of the flares. The plots display the averages for all events in the associated flare class. Flares outside of three standard deviations from the average and outside of 70° heliographic longitude are excluded. SHARP data are acquired from JSOC using the Python notebook created by Glogowski and Bobra (2016) and flare start times are identified by SWPC (2019).

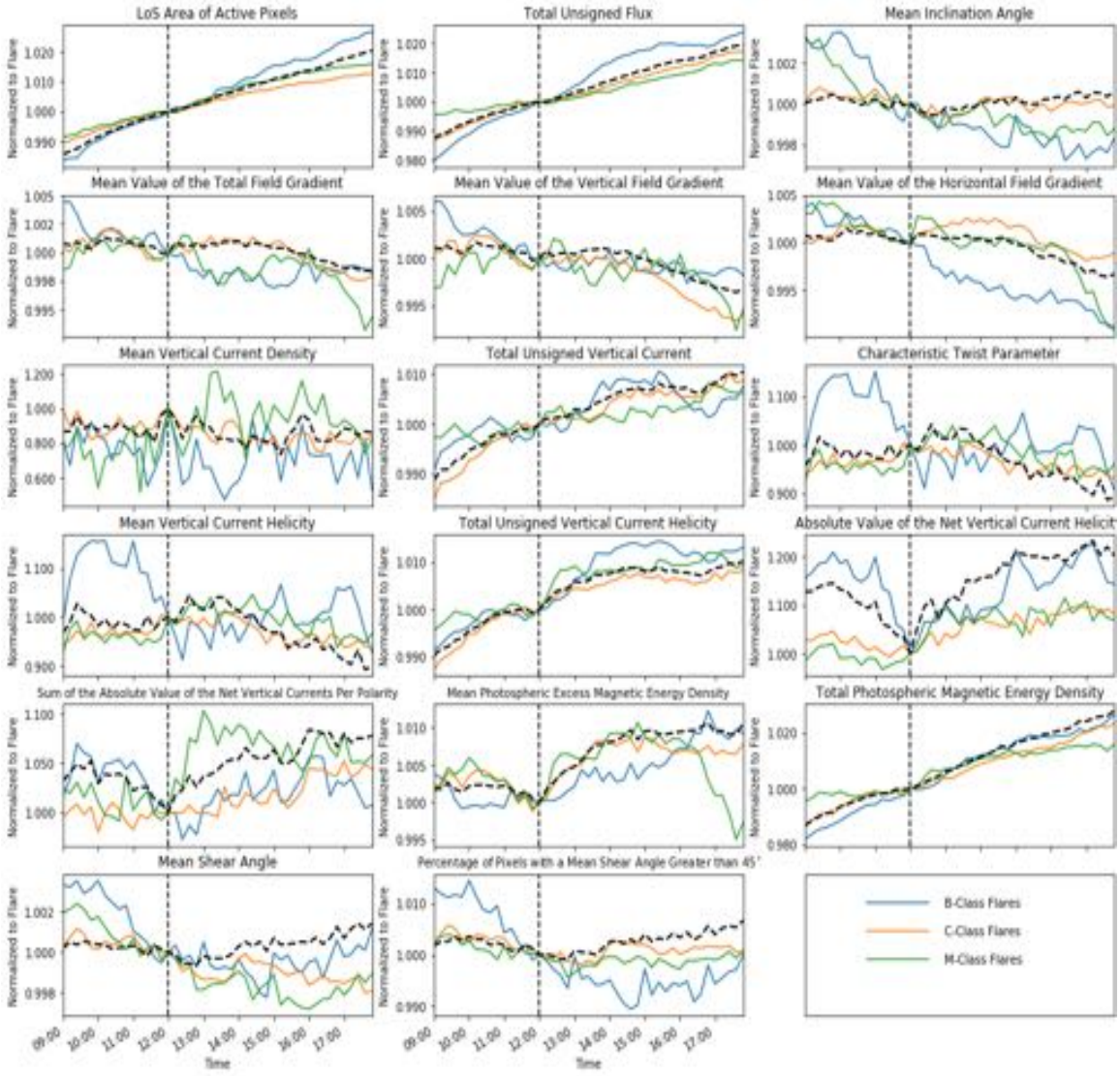

Figure 29. Epoch analysis for the 3-hour Precursor subset of flares without X-class data plotted. All data are normalized to the values at the start time of the flares. The plots display the averages for all events in the associated flare class. Flares outside of three standard deviations from the average and outside of 70° heliographic longitude are excluded. SHARP data are acquired from JSOC using the Python notebook created by Glogowski and Bobra (2016) and flare start times are identified by SWPC (2019).

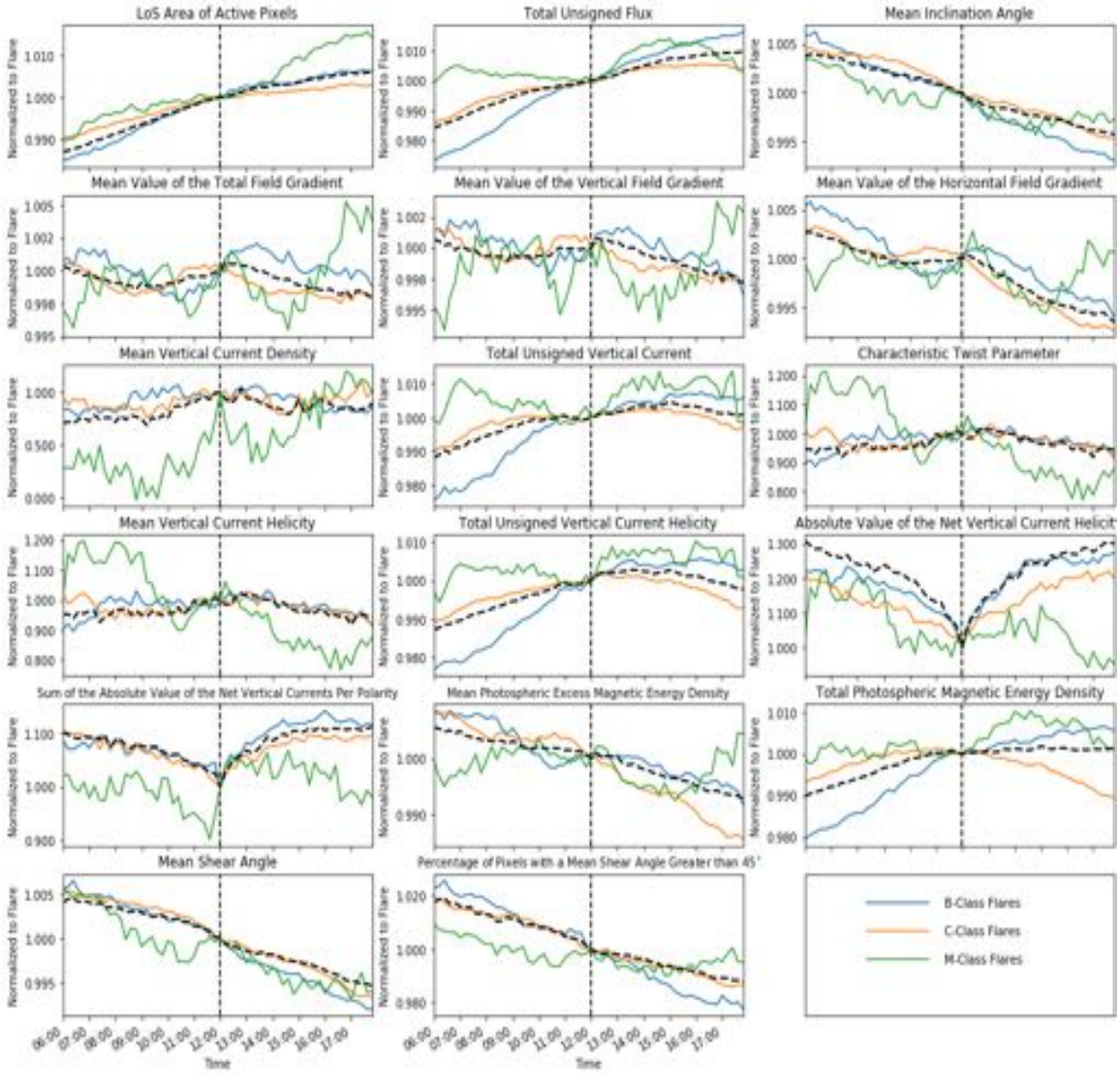

Figure 30. Epoch analysis for the 6-hour Non-Precursor subset of flares without X-class data plotted. All data are normalized to the values at the start time of the flares. The plots display the averages for all events in the associated flare class. Flares outside of three standard deviations from the average and outside of 70° heliographic longitude are excluded. SHARP data are acquired from JSOC using the Python notebook created by Glogowski and Bobra (2016) and flare start times are identified by SWPC (2019).

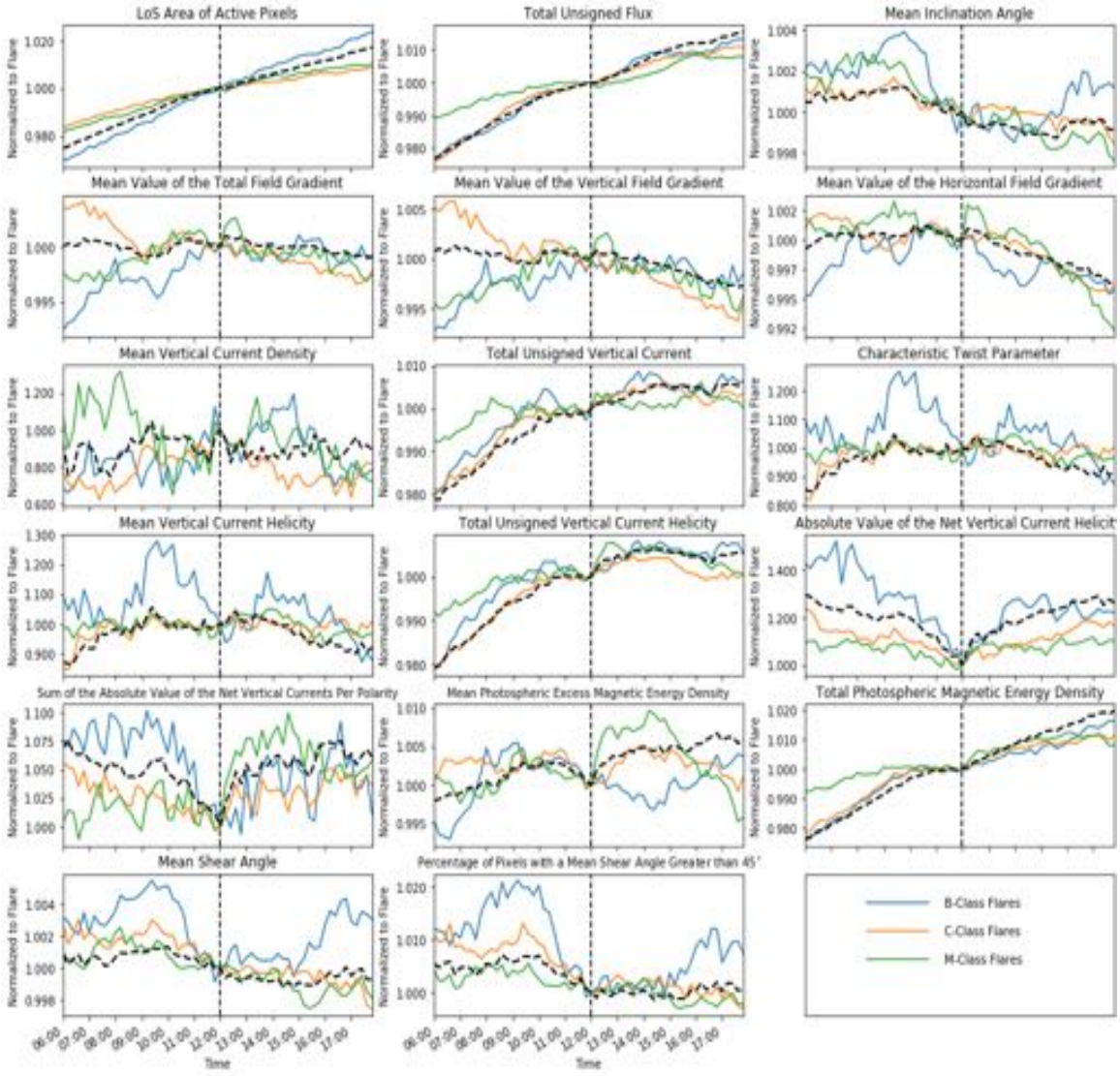

Figure 31. Epoch analysis for the 6-hour Precursor subset of flares without X-class data plotted. All data are normalized to the values at the start time of the flares. The plots display the averages for all events in the associated flare class. Flares outside of three standard deviations from the average and outside of 70° heliographic longitude are excluded. SHARP data are acquired from JSOC using the Python notebook created by Glogowski and Bobra (2016) and flare start times are identified by SWPC (2019).

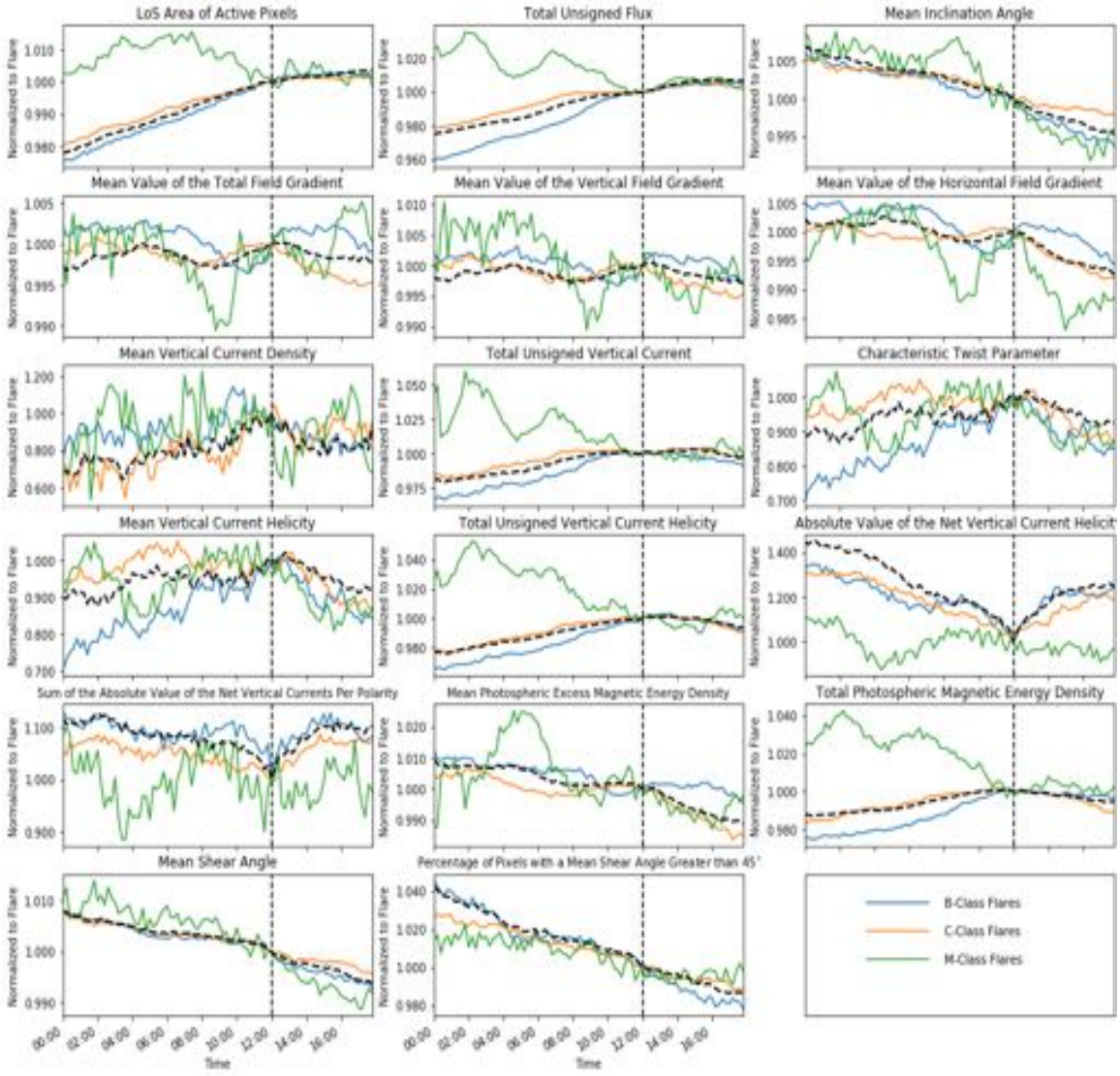

Figure 32. Epoch analysis for the 12-hour Non-Precursor subset of flares without X-class data plotted. All data are normalized to the values at the start time of the flares. The plots display the averages for all events in the associated flare class. Flares outside of three standard deviations from the average and outside of 70° heliographic longitude are excluded. SHARP data are acquired from JSOC using the Python notebook created by Glogowski and Bobra (2016) and flare start times are identified by SWPC (2019).

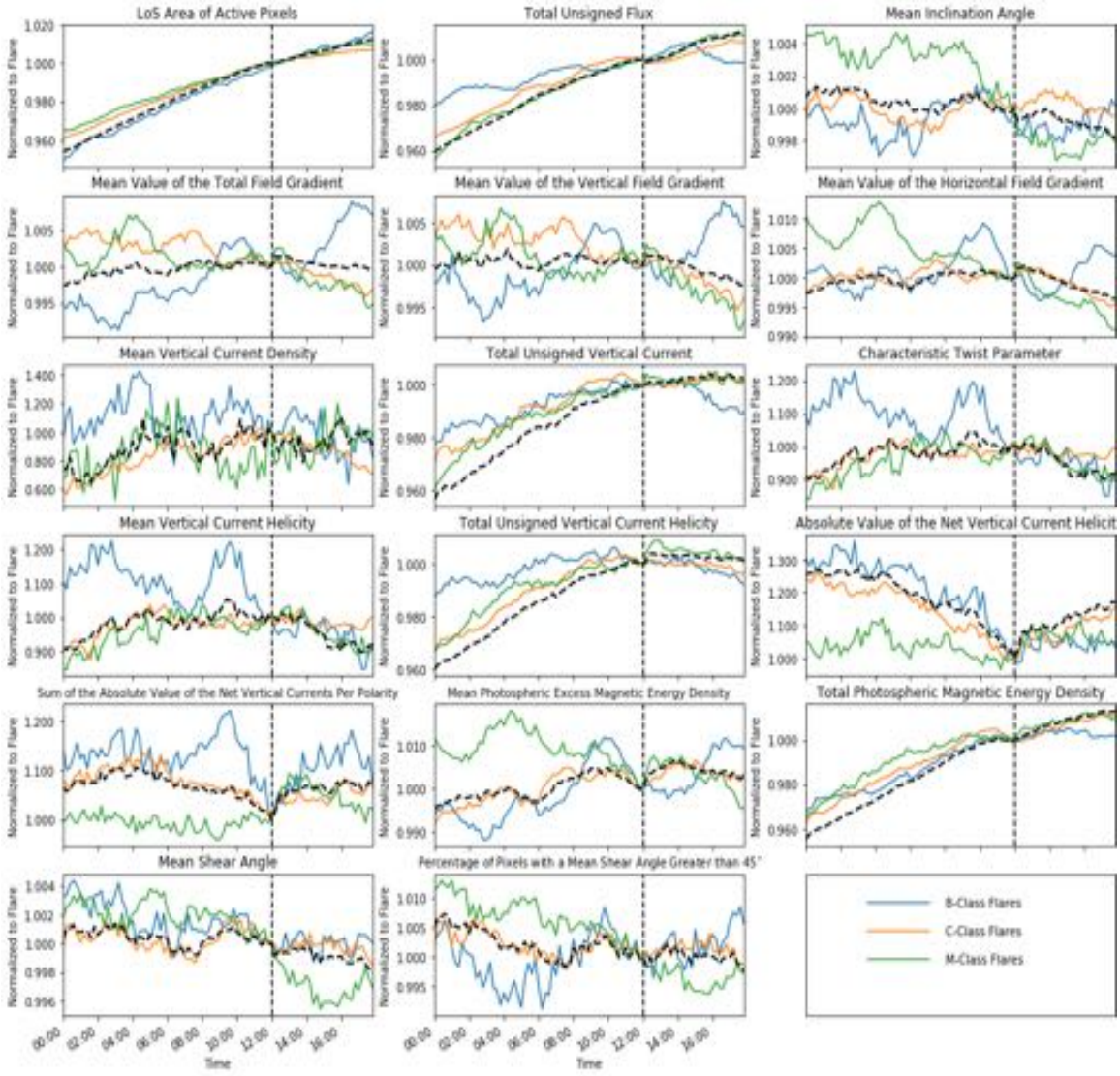

Figure 33. Epoch analysis for the 12-hour Precursor subset of flares without X-class data plotted. All data are normalized to the values at the start time of the flares. The plots display the averages for all events in the associated flare class. Flares outside of three standard deviations from the average and outside of 70° heliographic longitude are excluded. SHARP data are acquired from JSOC using the Python notebook created by Glogowski and Bobra (2016) and flare start times are identified by SWPC (2019).

Bibliography

Antiochos, S. and DeVore, C. R. (2008). The Role of Magnetic Reconnection in Solar Activity. In *37th COSPAR Scientific Assembly*, 37(1):102.

Barnes, G., Leka, K. D., Schrijver, C. J., Colak, T., Qahwaji, R., Ashamari, O. W., Yuan, Y., Zhang, J., McAteer, R. T. J., Bloomfield, D. S., Higgins, P. A., Gallagher, P. T., Falconer, D. A., Georgoulis, M. K., Wheatland, M. S., Balch, C., Dunn, T., and Wagner, E. L. (2016). A Comparison of Flare Forecasting Methods. I. Results from the "ALL-CLEAR" Workshop. *The Astrophysical Journal*, 829(2):89.

Bobra, M. G. and Couvidat, S. (2015). Solar Flare Prediction Using SDO/HMI Vector Magnetic Field Data with a Machine-Learning Algorithm. *The Astrophysical Journal*, 798(2):135.

Bobra, M. G., Sun, X., Hoeksema, J. T., Turmon, M., Liu, Y., Hayashi, K., Barnes, G., and Leka, K. (2014). The Helioseismic and Magnetic Imager (HMI) Vector Magnetic Field Pipeline: SHARPs – Space-Weather HMI Active Region Patches. *Solar Physics*, 289(9):3549-3578.

Chae, J., Choi, B.-K., and Park, M.-J. (2002). Chromospheric Magnetic Reconnection on the Sun. *Journal of Korean Astronomical Society*, 35:59-65.

Chae, J., Litvinenko, Y. E., and Sakurai, T. (2008). Determination of Magnetic Diffusivity from High-Resolution Solar Magnetograms. *The Astrophysical Journal*, 683(2):1153.

Eastwood, J., Biffis, E., Hapgood, M., Green, L., Bisi, M., Bentley, R., Wicks, R., McKinnell, L.-A., Gibbs, M., and Burnett, C. (2017). The Economic Impact of Space Weather: Where Do We Stand? *Risk Analysis*, 37(2):206-218.

Glogowski, K. and Bobra, M. G. (2016). A New Python Module for Accessing HMI and AIA Data. http://hmi.stanford.edu/hminuggets/?p=1757, last accessed on 1 September 2020.

Gyenge, N., Ballai, I., and Baranyi, T. (2016). Statistical Study of Spatio-Temporal Distribution of Precursor Solar Flares Associated with Major Flares. *Monthly Notices of the Royal Astronomical Society*, 459(4):3532-3539.

Hoeksema, J. T., Liu, Y., Hayashi, K., Sun, X., Schou, J., Couvidat, S., Norton, A., Bobra, M., Centeno, R., Leka, K., et al. (2014). The Helioseismic and Magnetic Imager (HMI) Vector Magnetic Field Pipeline: Overview and Performance. *Solar Physics*, 289(9):3483-3530.

Joint Science Operations Center (2020a). HARP - HMI Active Region Patches. http://jsoc .stanford.edu/jsocwiki/HARPDataSeries, last accessed on 30 November 2020.

Joint Science Operations Center (2020b). Science Data Processing. http://jsoc.stanford.edu/, last accessed on 11 December 2020.

Joint Science Operations Center (2020c). SpaceWeather HMI Active Region Patch (SHARP). http://jsoc.stanford.edu/doc/data/hmi/sharp/sharp.htm, last accessed on 30 November 2020.

Kazachenko, M. D., Lynch, B. J., Welsch, B. T., and Sun, X. (2017). A Database of Flare Ribbon Properties from the Solar Dynamics Observatory. I. Reconnection Flux. *The Astrophysical Journal*, 845(1):49.

Leka, K. and Barnes, G. (2003). Photospheric Magnetic Field Properties of Flaring versus Flare-Quiet Active Regions. II. Discriminant Analysis. *The Astrophysical Journal*, 595(2):1296.

Leka, K. and Barnes, G. (2007). Photospheric Magnetic Field Properties of Flaring versus Flare-Quiet Active Regions. IV. A Statistically Significant Sample. *The Astrophysical Journal*, 656(2):1173-1186.

Leka, K., Barnes, G., and Wagner, E. (2018). The NWRA Classification Infrastructure: Description and Extension to the Discriminant Analysis Flare Forecasting System (DAFFS). *J. Space Weather Space Clim.*, 8:A25.

Liu, J., Lin, C.-H., Tsai, H., and Liou, Y. (2004). Ionospheric Solar Flare Effects Monitored by the Ground-Based GPS Receivers: Theory and Observation. *Journal of Geophysical Research: Space Physics*, 109(A1).

Loper, R. (2018). \Reconnection Signatures in Solar Magnetograms". Proceedings of the 2018 AGU Fall Meeting. SH14B-04. Washington, D.C.: AGU, 2018.

Mason, J. and Hoeksema, J. (2010). Testing Automated Solar Flare Forecasting with 13 Years of Michelson Doppler Imager Magnetograms. *The Astrophysical Journal*, 723(1):634.

McIntosh, P. (1990). The Classification of Sunspot Groups. *Solar Physics*, 125(1):251-267.

Qian, L., Burns, A. G., Solomon, S. C., and Chamberlin, P. C. (2012). Solar Flare Impacts on Ionospheric Electrodyamics. *Geophysical research letters*, 39(6).

Priest, E. and Forbes, T. G. (2002). The Magnetic Nature of Solar Flares. *The Astronomy and Astrophysics Review*, 10(4):313-377.

Russell, C. T., Luhmann, J. G., & Strangeway, R. J. (2016). *Space Physics: An Introduction*. New York, NY: Cambridge University Press.

Sawyer, C., Warwick, J. W., & Dennett, J. T. (1986). Solar Flare Prediction. (Boulder, CO: Colorado Associated Univ. Press)

Scherrer, P. H., Schou, J., Bush, R., Kosovichev, A., Bogart, R., Hoeksema, J., Liu, Y., Duvall, T., Zhao, J., Schrijver, C., et al. (2012). The Helioseismic and Magnetic Imager (HMI) Investigation for the Solar Dynamics Observatory (SDO). *Solar Physics*, 275(1-2):207-227.

Schou, J., Scherrer, P. H., Bush, R. I., Wachter, R., Couvidat, S., Rabello-Soares, M. C., Bogart, R. S., Hoeksema, J. T., Liu, Y., Duvall, T. L., Akin, D. J., Allard, B. A., Miles, J. W., Rairden, R., Shine, R. A., Tarbell, T. D., Title, A. M., Wolfson, C. J., Elmore, D. F., Norton, A. A., and Tomczyk, S. (2012). Design and Ground Calibration of the Helioseismic and Magnetic Imager (HMI) Instrument on the Solar Dynamics Observatory (SDO). *Solar Physics*, 275(1):229-259.

Shibata, K. and Magara, T. (2011). Solar Flares: Magnetohydrodynamic Processes. *Living Reviews in Solar Physics*, 8(6).

Space Weather Prediction Center (2009). Implement XRS Event Detection. http://intranet /wiki/index.php?title=GOES-NOP:PPNCR0078&oldid=11361, last accessed on 24 September 2020.

Space Weather Prediction Center (2019). Data Archive. ftp://ftp.swpc.noaa.gov/pub/ warehouse/, retrieved on 25 September 2019.

Stanford University (2020). Helioseismic and Magnetic Imager. http://hmi.stanford.edu/ description/hmi-overview/hmi-overview.html, last accessed on 24 September 2020.

Verma, M. (2018). The Origin of Two X-Class Flares in Active Region NOAA 12673 Shear Flows and Head-on Collision of New and Preexisting Flux. *Astronomy & Astrophysics*, 612:A101.

Whitney, T. (2020). *Detection of Reconnection Signatures in Solar Flares* (Master's thesis). Air Force Institute of Technology, WPAFB, OH.

Whitney, T., Emmons, D., & Loper, R. (2020). Detection of Reconnection Signatures in Solar Flares. *Journal of Atmospheric and Solar-Terrestrial Physics*, 208, 105375.

Yamamoto, T. and Sakurai, T. (2009). Correlations between Flare Parameters and Magnetic Parameters in Solar Flares. *Publications of the Astronomical Society of Japan*, 61(1):75-84.

REPORT DOCUMENTATION PAGE

Form Approved
OMB No. 0704-0188

1. REPORT DATE *(DD-MM-YYYY)*	2. REPORT TYPE	3. DATES COVERED *(From - To)*
26-03-2021	Master's Thesis	May 2019 - March 2021

4. TITLE AND SUBTITLE

Studying the Conditions for Magnetic Reconnection in Solar Flares with and without Precursor Flares

5a. CONTRACT NUMBER

5b. GRANT NUMBER

5c. PROGRAM ELEMENT NUMBER

6. AUTHOR(S)

Garland, Seth H, Capt, USAF

5d. PROJECT NUMBER

5e. TASK NUMBER

5f. WORK UNIT NUMBER

7. PERFORMING ORGANIZATION NAME(S) AND ADDRESS(ES)

Air Force Institute of Technology
Graduate School of Engineering and Management (AFIT/EN)
2950 Hobson Way
Wright-Patterson AFB OH 45433-7765

8. PERFORMING ORGANIZATION REPORT NUMBER

AFIT-ENP-MS-21-M-117

9. SPONSORING/MONITORING AGENCY NAME(S) AND ADDRESS(ES)

Air Force Office of Scientific Research
Attn: Dr. Julie Moses
875 North Randolph Street, STE 325, Room 3112
Arlington, VA 22203
COMM 703-696-9586 Email: julie.moses@us.af.mil

10. SPONSOR/MONITOR'S ACRONYM(S)

AFOSR/RTB1

11. SPONSOR/MONITOR'S REPORT NUMBER(S)

12. DISTRIBUTION/AVAILABILITY STATEMENT

DISTRIBUTION STATEMENT A:
APPROVED FOR PUBLIC RELEASE; DISTRIBUTION UNLIMITED.

13. SUPPLEMENTARY NOTES

14. ABSTRACT

Forecasting of solar flares remains a challenge due to the limited understanding of the triggering mechanisms associated with magnetic reconnection, the primary physical phenomenon connected to these events. Consequently, methods continue to rely on the climatology of solar flare events as opposed to the underlying physics principles. Models of magnetic reconnection in the solar atmosphere places the null point of the reconnection within the corona. Though as of now the coronal magnetic field cannot be directly measured, the field is tied to the photospheric magnetic field, which can be. This study utilized data from the Solar Dynamics Observatory Helioseismic and Magnetic Imager and Space Weather HMI Active Region Patches to analyze full vector-field component data of the photospheric magnetic field during solar flare events within a near decade long dataset. Analysis of the data was used to compare the trends of differing flare classes for varying time intervals leading up to an event, as well as the trends of flares that occur with and without a precursor flare, in order to discern signatures of the physical mechanisms involved.

15. SUBJECT TERMS

Solar Photosphere, Solar Active Region Magnetic Fields, Solar Flares, Space Weather, Solar Magnetic Reconnection

16. SECURITY CLASSIFICATION OF:			17. LIMITATION OF ABSTRACT	18. NUMBER OF PAGES	19a. NAME OF RESPONSIBLE PERSON
a. REPORT	b. ABSTRACT	c. THIS PAGE			Dr. Robert D. Loper, AFIT/ENP
U	U	U	UU	87	19b. TELEPHONE NUMBER *(Include area code)* (937) 266-5506 robert.d.loper@nasa.gov